Elastic Inhomogeneity Effects on Microstructures

A Phase Field Study

A Thesis Submitted for the Degree of

Doctor of Philosophy

in the Faculty of Engineering

By

M. P. Gururajan

Department of Metallurgy

Indian Institute of Science

Bangalore – 560 012. INDIA

January 2006

To

My family and fiancée

Aththé, Annā, Ammā, Giri, Hema, Vasundhara, Rukmani, Raghav, Harini, and, Bhargavi

Acknowledgements

Feynmann (in one of his talks[1]) wishes the "good luck to be somewhere where you are free to maintain the kind of integrity" where one is true to oneself and others; I had such a luck working with Abi in the Computational Materials Science Group (CMSG). Almost all of what I learnt about research culture, research and its communication (be it writing, discussions or presentations), I owe to Abi. The present form of the thesis owes a lot to his help, encouragement, suggestions, guidance, and critical comments; many things that are said in this thesis (which are worth saying), are due to him.

I had extensive interactions with Prof. Jog of Mechanical Engineering department; his continuum mechanics course, and the discussions with him about the finite element method and homogenisation have been of immense help in my understanding the mechanical and mathematical aspects behind our phase field formulation. The inputs of Prof. Vijay Shenoy of Materials Research Centre helped me understand the formulation better.

I spent six wonderful months with Prof. Dr. Ferdinand Haider at the University of Augsburg, Augsburg. The discussions with Prof. Haider and others at EP-eins (especially Rolf Anders) about the atomic origins of elastic strains and their effect on phase separation were insightful and enjoyable.

I had thoroughly enjoyed my stay in the CMSG lab. The technical and non-technical discussions with Shankara were of more help than he realises. I learnt most of my elasticity, Fourier methods, and coding while doing two projects (as part of advanced phase transformations courses given by Abi) with Deep and Saswata as my project

[1] http://music.ls.huji.ac.il/members/nachum/feynman.html

partners. Ram brought his finite difference perspectives to our discussions. Their inputs along with those from Rajdip have helped me refine the thesis. Further, Ram, Shankara, Deep, Saswata, and Rajdip had read various sections of the thesis at various stages and helped me correct many an error and smoothen many a rough passage.

Sai and Pradeep of the Mechanical Engineering department gave me short tutorials on Maple which saved me days and days of painful algebra and helped me carry out some of the analytical calculations in a very reliable fashion.

My interactions with Dr. Sundararaman of BARC, Dr. Balamuralikrishnan of DMRL, Dr. SS Babu of WRI, Prof. Voorhees of North-Western University, Prof. Khachaturyan of Rutgers University, Prof. Roytburd of University of Maryland, Dr. Jin from Rutgers University, Prof. Kannan Krishnan of UCLA, Prof. Ramamoorthy Ramesh of UCB, and Prof. Vivek Shenoy of Brown have been informative, and encouraging. Dr. N. Sridhar of Rockwell centre, Prof. Dhanasekar, Central Queensland University, Australia, and Prof. Yoo and Dr. Yoon of Korea Advanced Institute of Science and Technology, obliged me with reprints, answered my queries, and clarified my doubts.

The members of the $\Sigma\tau$ group, especially, Prof. Ranganathan, Prof. Kamanio Chattopadhyay, and Prof. Vikram Jayaram gave me their comments and suggestions during my various presentations. I also had useful inputs from Dr. Karthikeyan.

The Chairmen of the Department Prof. Natarajan and Prof. Kamanio Chattopadhyay gave me access to all the departmental facilities (and funded my travels to conferences); the Chairman, SERC (and Mrs. Lakshmi) gave me access to their computing facilities. The financial assistance from CSIR, UGC-DAAD, and the Volkswagen Foundation at various stages of my stay at the Institute have been of great help.

Phani and Vichu, each in his own way, made me feel very happy about my work. Never did I come away from my meetings with them without learning some new technical stuff (and a bit of that malicious pleasure of life - gossip!).

Phaniraj has been my companion for almost everything that I enjoy; eating out,

movies, music, lectures, books, shopping, trekking, and chatting over coffee. His refreshingly cynical look at life (annoying, but never depressing) will be remembered for long; it was pleasant to have agreed him on issues; and pleasanter, when we disagreed. Along with him, Santa, Kotts, and Santa Singh would be the ideal companions that one can ask for a journey, especially, if the journey is as frustrating as writing a thesis. The coffees with them will sure to figure in my memoirs (if I ever write one).

The music lessons from, and discussions with (about life in general, and people in particular) *Pāttu Māmi* have been memorable. She opened a portal that would otherwise have been inaccessible – forever – to me . On a similar note, Bhaskar, Hariharan, and Guha brought immense joy with their music and discussions; my interactions with them enriched the experience of my stay at the Institute.

The innumerable students in the lab, Department and the Institute (as well as some others from Bangalore and elsewhere) have helped me in various ways. To have finished them all off, with a sentence at the least (or a paragraph at the most) is unjustified; however, my stay here had been long and I had known and interacted with far too many to list them all here. As I write this, I do remember each one of you, who have not been named!

I dedicate this thesis to my *family* and *fiancée*: Aththé, who is my teacher for the past twenty five years or more; Annā and Ammā, who patiently bore all my idiosyncrasies, unreasonable demands, eccentricities, and made me feel that what I am doing is important; Rukmani, Raghav, Giri and Hema, who took a lively interest in my research and showed me that there is fun outside the Institute campus too; Harini and Vasundhara, who never fail to amuse me (and decide to be amused by me once in a while, so that I do not feel out of place in their midst); and, Bhargavi, who brought me so much of joy with her (occasional) presence and (frequent) phone calls!

Contents

List of Tables

List of Figures

Notation

$\langle\{\cdot\}\rangle$	Volume average of the quantity $\{\cdot\}$ over the domain Ω (normalised by V)
$\{\{\cdot\}\}_{\mathbf{g}}$	Fourier transform of the quantity $\{\cdot\}$
A_Z	Average Zener anisotropy parameter; equals $2\overline{C}_{44}/(\overline{C}_{11} - \overline{C}_{12})$. When A_Z is unity, the system is elastically isotropic. When it is greater (or less) than unity, the system is elastically anisotropic with $\langle 10\rangle$ ($\langle 11\rangle$) directions being the soft directions
A_b	Constant that determines the energy barrier between the m and p phases in the bulk free energy density; more specifically, the energy barrier between the m and p phases is (1/16)th of A_b
α	Interpolation function for elastic modulus, a scalar function
a_p	Area of the precipitate
β	Interpolation function for eigenstrain, a scalar function

C Elastic modulus tensor; composition (and hence, position) dependent

C^{eff} The 'effective' elastic modulus tensor used for obtaining the zeroth order solution

C^m Elastic modulus tensor of the m phase

C^p Elastic modulus tensor of the p phase

$\overline{C}_{11}$ Circularly averaged Voigt constant C_{11}

$\overline{C}_{12}$ Circularly averaged Voigt constant C_{12}

$\overline{C}_{44}$ Circularly averaged Voigt constant C_{44}

c Composition (scaled)

c_0 Average alloy composition (in mole fraction of component B)

c_∞ Far-field composition

ΔC Difference between the elastic moduli of the p and m phases (a constant tensor)

Δc Effective supersaturation

δ Inhomogeneity; the ratio of the average shear modulus of the precipitate to that of the matrix. If δ equals unity, the precipitate is homogeneous. If δ is greater (less) than unity, the precipitate is harder (softer)

δ_{ij} Kronecker delta; equals unity if $i = j$ and zero otherwise

$\frac{\delta}{\delta c}$ Variational derivative with respect to composition

∇ Gradient operator (which is a vector operator)

$\partial\Omega$	Boundary of the simulation domain
E'	Characteristic energy used for non-dimensionalisation
$\mathbf{E}$	Homogeneous strain tensor; mean strain tensor of the simulation cell
ε	Total strain tensor
ε^0	Eigenstrain tensor (lattice parameter mismatch tensor)
ε^T	Strength of the eigenstrain; related to ε^0_{ij} through $\varepsilon^0_{ij} = \varepsilon^T \delta_{ij}$, where δ_{ij} is the Kronecker delta
$\varepsilon^\star$	Strain that is periodic on the domain Ω
ε^{el}	Elastic strain tensor
F	Total free energy of the system
F^{ch}	Chemical contribution to the free energy
F^{el}	Elastic contribution to the free energy
f_0	Bulk free energy density
G	Average shear modulus (equals $\overline{C}_{44}$)
G^{-1}	Acoustic tensor
G^m	Average shear modulus of the matrix phase
G^p	Average shear modulus of the precipitate phase
γ	Interfacial energy
$\mathbf{g}$	Fourier space vector

h_f Partial derivative of the bulk free energy density with respect to composition, $(\partial f_0/\partial c)$

J Imaginary number, $\sqrt{(-1)}$

κ Gradient energy coefficient

L' Characteristic length used for non-dimensionalisation

ℓ Characteristic length scale of a microstructure

M Mobility

μ Chemical potential (defined as the variational derivative of the total free energy)

N_V Number of atoms per unit volume

ν Average Poisson's ratio; equals $\overline{C}_{12}/(\overline{C}_{12}+\overline{C}_{44})$

Ω Simulation domain

R Equivalent radius; $\sqrt{a_p/\pi}$

ρ Aspect ratio of a rafted particle; defined as the diameter of the particle parallel to the applied stress direction to that perpendicular to the applied stress direction

S Compliance tensor, obtained from the inverse of the volume averaged elastic modulus tensor

σ^A Applied stress; should be such that the applied traction on the boundaries is anti-periodic

σ^T Eigenstrain tensor obtained by multiplying the strength of eigenstrain tensor (ε^T) by the effective elastic modulus tensor (C^{eff})

σ^{el} Elastic stress tensor

T' Characteristic time used for non-dimensionalisation

t Time

$\mathbf{u}$ Displacement field (from which the total strain is derived)

$\mathbf{u}^\star$ Displacement field that is periodic on the domain Ω

V Volume of the representational domain Ω

Chapter 1

Introduction

Elastic stresses arise during solid state phase transformations due to a lattice parameter mismatch (misfit) when the resultant phases are coherent. These stresses have a marked influence on the microstructural evolution: see the reviews [1–4]. Among these stress effects, some may be explained or rationalised using elastically homogeneous systems in which the phases have the same moduli. For some others, however, the difference in moduli (elastic inhomogeneity) is the primary cause. In this thesis, we consider the latter effects: rafting, phase inversion and thin film instability.

The following are some of the typical microstructural features observed in coherent two phase systems:

1. The precipitates change their shape as they grow in size, align along elastically soft crystallographic directions [5], and sometimes may even split [6–8];

2. The elastic stresses interact with externally applied uniaxial stresses which results in 'rafting', viz., the preferential coarsening of the precipitates either parallel or perpendicular to the direction of applied stress [9];

3. In a thin film assembly, if the film is harder than the substrate, that can lead to instabilities in the film (which is known as the 'Asaro-Tiller-Grinfeld' instabilities [10]).

In addition, several simulation studies suggest that a microstructure consisting of

soft precipitates in a hard matrix can evolve into one of hard precipitates in a soft matrix; this is known as 'phase inversion' [11].

Of the microstructural features listed above, alignment and shape changes of the precipitates can be satisfactorily explained assuming the precipitate and matrix phases to have the same elastic constants; the effect of elastic moduli mismatch between the two phases, if any, is negligible. On the other hand, in all the other cases, the elastic moduli mismatch between the two phases plays a key role: rafting in systems with dilatational misfit, phase inversion and Asaro-Tiller-Grinfeld instabilities will not be observed in systems in which all the phases have identical elastic constants.

The modelling studies of microstructural evolution in elastically inhomogeneous, coherent systems can broadly be classified as continuum and atomistic studies. In continuum studies, the microstructure is described using field variables (like composition, for example), in contrast to atomistic models where site occupancy on a lattice is used to describe the system. While continuum models are based on classical field theories, the atomistic models are based on (classical) statistical mechanics [3].

The continuum studies are further subdivided into sharp and diffuse interface studies; in sharp (diffuse) interface models, the field variables vary discontinuously (continuously) across an interface. The diffuse interface models are also known as phase field models [3].

The sharp interface models are typically used to obtain analytical results and for carrying out perturbation/stability analyses. The analytical results are usually obtained under the assumptions of simple geometry, single particle in an infinite matrix, and/or isotropic elasticity. Many of these restrictive assumptions can be relaxed, if, numerical methods based on these sharp interface methods are used. Even in such circumstances (since sharp interface models track interfaces explicitly) singularities arise due to merger or disappearance of microstructural features. Since such singularities are difficult to handle in a numerical scheme, sharp interface models have been only of limited use [3, 12].

Diffuse interface models on the other hand are ideal for the study of multiparticle microstructures, complex geometries, anisotropic elastic parameters, and interface singularities. However, the results from the diffuse interface models always need

to be benchmarked against the corresponding sharp interface models; further, the definitive interface width in these models can lead to difficulties in simulating large scale microstructures [12].

In this thesis, our emphasis is on continuum diffuse interface studies. The existing phase field studies of microstructural evolution in elastically inhomogeneous, coherent, misfitting systems are of relatively recent origin. Some of these studies assume the difference in the elastic moduli (ΔC) between the two phases to be small [11, 13–17]. In contrast, the microstructural evolution in systems with large differences in elastic moduli (where higher order corrections are incorporated) has been studied by Leo et al [18], Zhu et al [19] and Hu and Chen [20].

Almost all the phase field studies on microstructural evolution in systems with large differences in elastic moduli, solve the equation of mechanical equilibrium under conditions of prescribed displacement [16,19,20]. Such a boundary condition, though natural in the study of microstructural evolution in thin films for example, is not satisfactory in cases (a) where the system evolves under the action of an externally applied stress, or, (b) where the system evolves with no tractions or constraints on displacements at the boundary.

Further progress in the study of elastically inhomogeneous systems needed an accurate and computationally viable technique for solving for elastic stresses in these systems with arbitrary microstructures and prescribed external tractions. There are at least two possibilities. The first is due to Khachaturyan and his coworkers in which an equivalent eigenstrain which minimises the strain energy of the corresponding elastically homogeneous system is calculated using a non-conserved order parameter of Allen-Cahn type [21–24].

The second approach, which we have adapted in this study, is from the literature on "homogenisation" [25–27]. In this approach, a system which is elastically inhomogeneous is replaced by a system of 'equivalent' (homogeneous) elastic moduli. The main ingredient in such a calculation is a consistent calculation of the homogeneous strain [25,26]; the algorithm for such a consistent calculation (for prescribed traction boundary conditions) is known as 'stress-control using strain-control' approach and is described in Section 3.2.

The main emphasis of the homogenisation studies is on the calculation of homogeneous moduli, while our interest is in the study of microstructural evolution in elastically inhomogeneous systems in the presence of eigenstrains. So, we have adapted the solution method to a coherent system with misfit strains; we incorporate the resultant elastic solutions into a phase field model. Such a phase field model then allows us to study microstructural evolution in elastically inhomogeneous coherent solids under conditions of prescribed tractions at the boundary. We demonstrate the efficacy of the solution technique by comparing our numerical elastic solutions for (a) misfitting precipitates and (b) cavities under uniaxial stress with the corresponding analytical sharp interface results.

We have used this technique to study two different phenomena in bulk systems with dilatational misfit: (a) rafting in systems with dilatational misfit, and (b) phase inversion. In the case of rafting, the system evolves under an externally applied stress, while in the case of phase inversion, the boundaries are free from both the traction and displacement constraints.

Though our emphasis in this thesis is on bulk systems which evolve under prescribed traction conditions, our numerical method can also be used for the study of microstructural evolution in systems with prescribed displacement boundary conditions: see Appendix **??** where we show some of our preliminary results on ATG instabilities in thin film assemblies.

Our formulation as described in Chapter 3 is valid for three dimensional (3D) elasticity; however, the numerical simulations are carried out in two dimensions (2D). Typically, elastic fields in such 2D simulations are calculated using a 3D formulation assuming plane strain conditions to hold. In contrast, in this thesis, we use a pure 2D elastic calculation.

This thesis is organised as follows: in the next chapter, we summarise the typical microstructural features observed in elastically inhomogeneous systems. In Chapter 3, we describe the diffuse interface formulation; the emphasis in this chapter is on the validation and characterisation of our numerical method for solving for elastic stresses in inhomogeneous systems. In Chapter **??** and Chapter **??** we describe our simulation results from the studies on rafting and phase inversion, respectively. Our

results on ATG instability are preliminary, and are described briefly in Appendix **??**. We conclude the thesis with a brief summary in Chapter **??**.

Chapter 2

Microstructural evolution in elastically stressed solids: a review

The literature on the effect of elastic stresses on phase transformations, nucleation, growth, microstructural evolution, and mechanical properties are vast, rich, and varied: see the excellent monographs [28–31], and reviews [1–4, 32, 33]. In this chapter, we summarise the studies on the microstructural evolution in elastically stressed solids with an emphasis on those microstructural features that result due to elastic inhomogeneities. Thus, for example, thermodynamics of elastically stressed systems, and problems of equilibrium shapes of precipitates in elastically stressed systems will not be discussed here. While the salient features in elastically inhomogeneous systems are described here, the individual chapters on formulation, rafting, and phase inversion carry their own detailed literature surveys.

Almost all the experimental studies described in this chapter are electron microscopic studies. The modelling studies may broadly be classified as continuum and atomistic studies. The continuum studies are further classified as sharp and diffuse interface studies. The results from the sharp interface and atomistic models are discussed in this survey in so far as they concern the study of microstructural evolution in elastically inhomogeneous systems; however, since we use a diffuse interface model in this thesis, we give a brief overview of the same in Section 2.6.

We define the elastic inhomogeneity δ to be the ratio of the shear modulus of the

precipitate to that of the matrix:

$$\text{inhomogeneity, } \delta = \frac{G^p}{G^m} \tag{2.1}$$

Experimentally, the determination of the elastic constants is quite difficult, particularly at high temperatures. In Ni-Al systems, for example, their values are disputed and the exact value of δ is not known [34]. Further, it is not even clear whether δ is greater or less than unity; that is, as to whether the precipitate phase is harder or softer [35]. These differences in the interpretations of experimental results stem from the fact that composition, additional alloying elements, temperature, and the heat treatment affect the measurement of elastic moduli, and it is well near impossible to keep all these quantities identical across different experimental studies. Hence, the only conclusion that can be drawn from all these studies is that δ is not unity. Thus, all the experimental studies can, in principle, be considered to be carried out on inhomogeneous systems. However, as we discuss below, several theoretical and modelling studies help us identify the cases in which the effect of inhomogeneity is primary.

2.1 Particle shape change and alignment

In a classic study on coherent Ni_3Al (γ') precipitates in a Ni-rich (γ) matrix, Ardell and Nicholson [5] have shown that the precipitates (a) change their shape with increasing size, and (b) align themselves along the elastically softer directions. The primary driving force for shape change is the decrease in elastic strain energy while, that for alignment is the anisotropy in the elastic constants [36, 37]. However, the role of elastic inhomogeneities on shape change and alignment is not clear from these experiments.

Particle shape changes are driven by the competition between the interfacial and elastic energies; hence the role of δ is secondary. For example, studies by Wang et al [38], and Wang and Khachaturyan [39], show clearly that particle shape change will occur even if δ is unity. Similarly, there are several diffuse interface studies which show that the elastic anisotropy, even in the absence of any elastic inhomogeneities, can lead to alignment of the misfitting precipitates along elastically softer

directions [15, 38].

The typical shape changes observed during growth of a precipitate are circle-to-square transitions (sphere to cuboid transitions in 3D), which are driven by the elastic energy anisotropy [39]. Similarly, Leo et al [18], show that the same sized elliptic particle, depending on the relative strength of elastic strain energy might remain as an ellipse or turn into a circle. We are not aware of any study in which a growing isotropic (anisotropic) precipitate undergoes a circle-to-ellipse (square-to-rectangle) transition. The reason for this, though not yet established conclusively, could be (1) mechanistic or kinetic, viz., the difficulty in choosing one direction over another [See the atomistic simulations of Lee [40] for example, and the intermediate shapes that are observed in his simulations], and (2) energetic, viz., the driving force for shape change as compared to that for growth is very small under growth conditions.

2.2 Particle splitting, coalescence, and morphological instabilities

Particle splitting has been reported [6–8, 41–43] in several systems. However, the interpretation of these experimental observations is disputed by Calderon et al [44]; Calderon et al show that coalescence of particles can give rise to morphologies similar to splitting patterns. Further, Yamabe-Mitarai and Harada [45], attribute particle splitting to a kinetic phenomenon associated with the deviation of the precipitate composition from its equilibrium composition. Thus, experimentally, though it is clear that particles do split and coalesce, the driving forces and mechanisms of splitting are also yet to be conclusively established. Further, the effect of δ, if any, on the particle splitting and/or coalescence is not clear from these experimental studies.

Energetically, both Doi [6, 42] and Khachaturyan et al [46] have shown the dependence of doublet, quartet, and octet particle splitting on particle size. However, the simulations of particle splitting during the growth of elastically stressed particles are inconclusive. In the simulations of Wang et al [38], the matrix nucleates

at the centre of the precipitate, and grows, resulting in a doublet; but this type of splitting could be an artifact of the simulation itself. The initial particle size, under the given elastic parameters, is such that the levels of elastic stress at the centre of the precipitates are unphysically high, leading to the nucleation of the matrix (and hence splitting). On the other hand, Banerjee et al [47], show that particle coalescence (in both 2- and 3-D simulations) can lead to aggregation of particles that gives rise to microstructural features that look like doublet, quartet and octet split patterns. While the instabilities that arise during growth do not lead to particle splitting in the simulations of Wang and Khachaturyan [39], similar growth related instabilities lead to particle splitting in the simulations of Cha et al [48]. All the studies listed above (except Cha et al) are studies on elastically homogeneous systems; thus, apart from concluding that the particle splitting and/or coalescence can happen even in elastically homogeneous systems, the effect of δ on particle splitting and/or coalescence, if any, is not clear from these simulation studies.

In some Ni-base alloys, as a γ' precipitate grows into a supersaturated γ matrix, the precipitate/matrix interface may undergo instabilities [8, 49]; the observations of Yoo et al [8] further indicate that the anisotropy in the elastic moduli as well as particle splitting may have a role in producing such dendritic morphologies.

The elastic inhomogeneity may have a role in the development of morphological instabilities [50]. On the other hand, the study of Yeon et al [51] indicates that even in elastically homogeneous systems the morphological instabilities can occur. Thus, from these studies also the effect of δ on morphological instabilities is not clear.

Thus, morphological instabilities and particle splitting/coalescence occur in elastically stressed particles growing in a supersaturated matrix. However, the driving forces and the mechanisms of particle splitting, as well as the effect of elastic inhomogeneity on splitting, coalescence, and morphological instabilities, both in experiments and in simulations, are yet to be investigated completely.

2.3 Rafting

In a classic study, Tien and Copley [9], showed that an uniaxial stress leads to preferential coarsening of γ' precipitates parallel or perpendicular to the direction of applied uniaxial stress in nickel-base superalloy single crystals; this phenomenon is known as rafting.

In systems with dilatational misfit, several studies have shown that the driving force for rafting goes to zero as δ approaches unity [52–56]. Thus, elastic inhomogeneity is an essential requirement for rafting in systems with dilatational misfit. Phase field simulations of rafting have been reported by Zhu et al [19], Leo et al [18], Li and Chen [16], while atomistic simulations of rafting has been reported by Lee [57]. However, if the eigenstrains are non-dilatational, elastic inhomogeneity is not essential for the occurrence of rafting [58].

2.4 Phase inversion

In two phase microstructures, the higher volume fraction usually percolates with distributed isolated islands of the lower volume fraction. The percolating phase is the 'matrix' while the distributed phase is the 'precipitate'. However, in some systems, this correspondence between the volume fraction and topological structure is reversed. More specifically, an initial microstructure in which the higher volume fraction phase percolates, evolves into one in which the lower volume fraction phase percolates. This is known as 'phase inversion'. Such a phase inversion is reported in both experimental and numerical studies on phase separating viscoelastic polymer blends (See [59] and references therein). In elastically stressed systems, phase inversion is said to occur when a microstructure consisting of soft precipitates in a hard matrix evolves into one of hard precipitates in a soft matrix; such purely elasticity driven phase inversion have been reported in several (albeit restrictive) computational studies [11, 18, 60]. However, we are not aware of any experimental report of such an elasticity driven inversion.

2.5 Thin film and surface instabilities

The surfaces and interfaces of non-hydrostatically stressed crystalline solids are found to be unstable with respect to perturbations. Such instabilities have been widely reported [61–63]: see [4,64,65] for a summary of experimental results. These instabilities differ from the dendritic instabilities discussed in Section 2.2; while dendritic instabilities are growth related, the thin film and surface instabilities can be observed in the absence of growth and are related to the equilibrium shape of non-hydrostatically stressed solids [66].

In the thin film literature, these elastic stress driven surface and interface instabilities are known as Asaro-Tiller-Grinfeld (ATG) instabilities following the independent prediction of such instabilities by Asaro and Tiller [67] and Grinfeld [68]. While Asaro-Tiller-Grinfeld studied the instability of a solid-liquid interface, Srolovitz [69] showed that a solid-vapour interface can also undergo an ATG-like instability. Further, Sridhar et al [10] have shown ATG-like instabilities to occur even in a solid-solid interface, as long as the harder (film) phase is embedded in a soft (matrix) phase. Thus, ATG instabilities are driven by elastic inhomogeneities; they will not occur in systems in which the interface is shared by two phases with the same elastic constant.

2.6 Diffuse interface modelling

In a continuum model for the study of two phase microstructures, there are two distinct ways of treating the interfaces. Based on the manner in which the interface is described, these models are classified into two types, namely, sharp interface models and diffuse interface models. In the former, the interface is a plane of discontinuity across which the properties change abruptly from that of one phase to another. In the later, the interface width is not determined a priori, and the properties change over a definite width from that of one phase to another in a smooth fashion.

While the sharp interface approach was pioneered by Gibbs [70], a diffuse interface model was formulated by Cahn [71, 72] to study spinodal decomposition, in which,

the interfaces that form during the early stages are indeed compositionally diffuse. The treatment of Cahn was based on the free energy functional for a compositionally nonuniform system; such a free energy functional was derived by Cahn and Hilliard [73]. Hence, these models based on composition fields (and gradients in composition) are known as Cahn-Hilliard models. However, in systems which undergo an order-disorder transformation for example, the microstructure is described by field parameters which are not conserved (unlike the composition field). The diffuse interface models based on such non-conserved order parameter fields, following the work of Allen and Cahn [74] are known as Allen-Cahn equations. Hybrid models based on both Cahn-Hilliard and Allen-Cahn equations are also possible.

The main advantage of numerical studies based on the Cahn-Hilliard and/or Allen-Cahn equations stem from the fact that the field parameters that describe the microstructure (as well as their higher order spatial derivatives) are continuous everywhere. Hence, the partial differential equations which describe the microstructural evolution hold in the entire simulation domain; thus, there is no need to track the interface explicitly. On the other hand, sharp interface based numerical models track the interface explicitly; hence, they are incapable of treating singularities that arise due to the formation or disappearance of interfaces.

The diffuse interface models based on the Cahn-Hilliard and Allen-Cahn equations are used for the study of microstructural evolution in a wide variety of problems: see [12, 75, 76] for recent reviews.

In this thesis, we base our diffuse interface model on the Cahn-Hilliard equation; we modify the system energetics to include the elastic energy contributions. The elastic energy is obtained by solving the elastic field equations in an elastically inhomogeneous system under prescribed traction or displacement boundary conditions. The formulation is described in detail in Section 3.1.

2.7 Summary

Some of the typical microstructural features observed in elastically stressed solids are as follows: particle shape change, alignment, splitting/coalescence, morphological

instabilities, rafting, phase inversion, and ATG instabilities. Of these, the elastic inhomogeneity plays a crucial role in rafting, phase inversion, and ATG instabilities, while the effect of elastic inhomogeneity, if any, on particle shape change, alignment, splitting/coalescence, and morphological instabilities are weak and secondary.

Chapter 3

Formulation

Phase field methods based on the Cahn-Hilliard and/or Allen-Cahn equations are used extensively for the study of microstructural evolution in elastically stressed solids; see the reviews by Chen [75] and Thornton et al [12]. In these models, the elastic stress effects are typically incorporated by adding an elastic energy term to the free energy. The calculation of the elastic energy involves the solution of the equation of mechanical equilibrium, which is typically solved (in elastically inhomogeneous systems) using pseudo-spectral techniques [18] (which are a combination of finite difference and Fast Fourier Transform (FFT) techniques), (pre-conditioned) conjugate gradients [19] or spectral techniques based on FFT [20–22]. In this thesis, we use a diffuse interface model based on the Cahn-Hilliard equation for the study of microstructural evolution in elastically inhomogeneous systems under either prescribed displacement or prescribed traction boundary conditions. The equation of mechanical equilibrium is solved using an iterative method based on Fourier transforms. A semi-implicit Fourier spectral method is used for solving the Cahn-Hilliard equation.

The diffuse interface model and the iterative procedure for solving the equation of mechanical equilibrium are known in the literature [19–24]. However, in most of these studies, the equation of mechanical equilibrium is not solved under conditions of applied tractions [20]; in cases where they are solved, the homogeneous strain is not calculated in a consistent manner [19]. On the other hand, a method of

obtaining the homogeneous strain is described in the diffuse interface literature by Wang et al [24], and in the homogenisation literature by several others [25–27]. More specifically, in the homogenisation literature, the algorithm for a consistent calculation of homogeneous strain under applied traction conditions is described in great detail (See appendix D of [26], for example).

In Section 3.1, we recount the salient features of the Cahn-Hilliard model, in which the total free energy is written as a simple sum of chemical and elastic contributions (each of which is microstructure dependent). In Section 3.2, we recount the equation of mechanical equilibrium and the constraints and boundary conditions under which it needs to be solved.

Section 3.3 is central to this chapter, as it deals with with an iterative numerical technique for solving the equation of mechanical equilibrium in elastically inhomogeneous systems. The technique, adapted from the homogenisation literature [25, 26], is efficient and accurate: there are no approximations about the extent of modulus mismatch and solutions with both prescribed traction and displacement boundary conditions are possible.

In Sections 3.4, 3.5, and 3.6, we describe the calculation of the elastic energy (and hence the elastic part of the chemical potential), the non-dimensionalisation and the details of numerical implementation, respectively.

In Section 3.7, we compare our numerical elastic solutions with the corresponding analytical, sharp interface solutions for (a) circular and elliptic precipitates (Section 3.7.1), and (b) circular cavities in a square plate under a tensile stress (Section 3.7.2). Further, these comparisons are used in Section 3.8, (a) to characterise the numerical method in terms of the effect of various simulation parameters on the accuracy of the elastic solutions and (b) the efficiency of the numerical method. In Section 3.9 we present some results from homogeneous strain and homogeneous moduli calculations in systems with simple geometries, namely, circular precipitates in a square domain. Finally, we end the chapter with a brief summary.

3.1 The Cahn-Hilliard equation with modified free energy

We consider a binary phase separating A-B alloy system exhibiting a miscibility gap. At a low temperature (say T), any alloy of composition c'_0 that finds itself inside the miscibility gap will consist of two phases m and p with compositions c'_m and c'_p, respectively, at equilibrium (see Figure 3.1).

We rescale the composition variable c' to yield the scaled composition c:

$$c = \frac{c' - c'_m}{c'_p - c'_m}. \tag{3.1}$$

With this definition, c is the same as the equilibrium volume fraction of the p-phase; in particular c takes a value of zero and unity in the matrix and precipitate phases, respectively. Further, all the variables are rendered non-dimensional using a characteristic length L', energy E', and time T', a suitable choice for which is deferred to section 3.5. All the equations in our formulation, are presented in terms of non-dimensional and scaled variables; the dimensional forms of the corresponding equations are shown in Appendix A.

Let the composition at any point $\mathbf{r}$ at time t be denoted by $c(\mathbf{r}, t)$. Let the microstructure of the system be completely described by the composition field. Consider a domain Ω bounded by $\partial\Omega$ of such a system; we assume the composition field to be periodic on Ω, i.e., Ω is the representative region that repeats infinitely to fill all space (see Figure 3.2). This assumption of periodicity helps us avoid accounting for the surfaces in our calculations.

Given an initial microstructure (i.e., composition profile), say c($\mathbf{r}$,0), its future evolution can be studied by solving the following Cahn-Hilliard equation (with periodic boundary conditions) [71]:

$$\frac{\partial c}{\partial t} = \nabla \cdot M \nabla \mu, \tag{3.2}$$

where, M is the mobility, c is the (scaled) composition, t is the time, and μ is the chemical potential, given by

$$\mu = \frac{\delta \left[\frac{F}{N_V} \right]}{\delta c}, \tag{3.3}$$

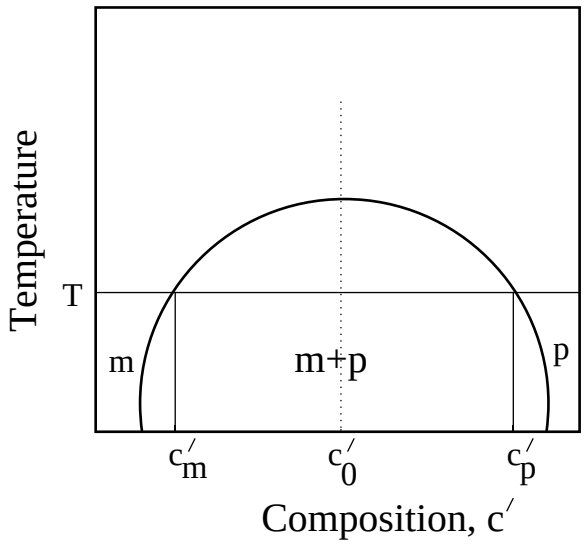

Figure 3.1: Schematic phase diagram of a phase separating system: c_0' is the alloy composition; c_m' and c_p' are the equilibrium compositions of the m and p phases at the temperature T.

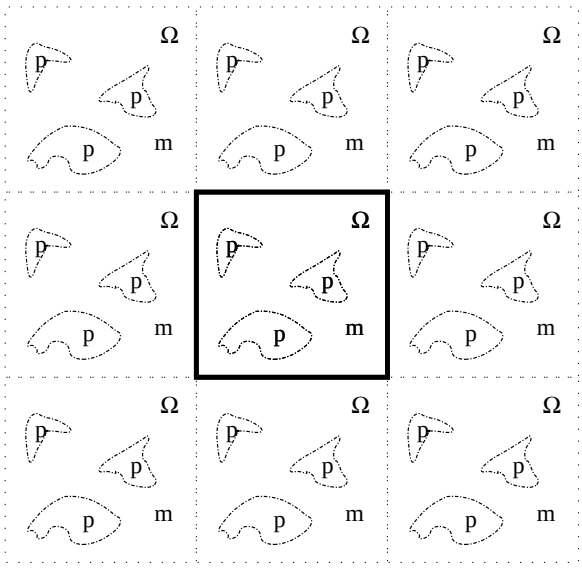

Figure 3.2: The simulation domain Ω; the periodic boundary conditions are indicated by the dotted lines.

where $(\delta/\delta c)$ denotes the variational derivative with respect to composition, N_V is the number of atoms per unit volume. The total free energy of the system, F, is assumed to be of the form

$$F = F^{ch} + F^{el}, \tag{3.4}$$

where F^{ch} and F^{el} are the chemical and elastic contributions to the free energy; in other words the state of stress has a negligible effect on F^{ch}. Substituting this free energy expression in Eqn. (3.3), we obtain the (modified) Cahn-Hilliard equation as follows:

$$\frac{\partial c}{\partial t} = \nabla \cdot M\nabla(\mu^{ch} + \mu^{el}), \tag{3.5}$$

where,

$$\mu^{ch} = \frac{\delta\left[\frac{F^{ch}}{N_V}\right]}{\delta c}, \tag{3.6}$$

and,

$$\mu^{el} = \frac{\delta\left[\frac{F^{el}}{N_V}\right]}{\delta c}. \tag{3.7}$$

The chemical contribution to the free energy is given by the following expression:

$$F^{ch} = N_V \int_\Omega [f_0(c) + \kappa(\nabla c)^2] d\Omega, \tag{3.8}$$

where, κ is the gradient energy coefficient, and $f_0(c)$ is the bulk free energy density given by

$$f_0(c) = A_b c^2(1-c)^2, \tag{3.9}$$

where A_b is a positive constant which sets the energy barrier between the two equilibrium phases m and p (see Figure 3.3); thus,

$$\mu^{ch} = h_f(c) - 2\kappa\nabla^2 c, \tag{3.10}$$

with, $h_f(c) = (\partial f_0/\partial c)$.

In this thesis, we assume the mobility M in Eqn. (3.2) and the gradient energy coefficient κ in Eqn. (3.8) to be (scalar) constants: this amounts to assuming the interfacial energies and the diffusivities to be isotropic.

The elastic contribution to the free energy is [75]:

$$F^{el} = \frac{1}{2}\int_\Omega \sigma_{ij}^{el}\varepsilon_{ij}^{el} d\Omega \tag{3.11}$$

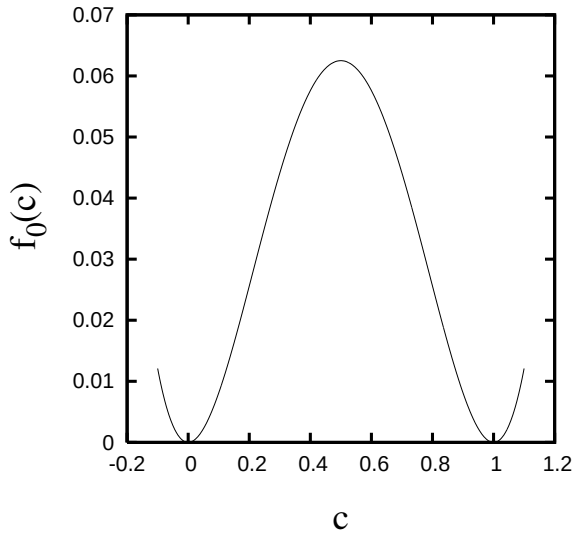

Figure 3.3: The bulk free energy density (with $A_b = 1$). The equilibrium compositions for the m and p phases are at zero and unity, respectively. The barrier height between the m and p phases is $(A_b/16)$.

where,

$$\varepsilon_{ij}^{el} = \varepsilon_{ij} - \varepsilon_{ij}^{0}, \tag{3.12}$$

with ε^0 being the position dependent eigenstrain (misfit strain) tensor field; and, the total strain ε_{ij} is compatible:

$$\varepsilon_{ij} = \frac{1}{2}\left\{\frac{\partial u_i}{\partial r_j} + \frac{\partial u_j}{\partial r_i}\right\}, \tag{3.13}$$

where $\mathbf{u}$ is the the displacement field, and, (assuming both the m and p phases to obey Hooke's law i.e., the phases are linear elastic)

$$\sigma_{kl}^{el} = C_{ijkl}\varepsilon_{ij}^{el}, \tag{3.14}$$

where C_{ijkl} is the composition (and hence, position) dependent elastic modulus tensor.

The eigenstrain is an explicit function of composition and is described by

$$\varepsilon_{ij}^{0}(c) = \beta(c)\varepsilon^{T}\delta_{ij}, \tag{3.15}$$

where, ε^T is a constant that determines the strength of the eigenstrain, δ_{ij} is the Kronecker delta, and $\beta(c)$ is a scalar function of composition. The elastic modulus tensor is also an explicit function of composition; in other words, the solid is

elastically inhomogeneous. The composition dependence of the elastic constants is described by the following expression:

$$C_{ijkl}(c) = C^{\text{eff}}_{ijkl} + \alpha(c)\Delta C_{ijkl}, \tag{3.16}$$

where $\alpha(c)$ is a scalar function of composition, and,

$$\Delta C_{ijkl} = C^{p}_{ijkl} - C^{m}_{ijkl} \tag{3.17}$$

where, C^{p}_{ijkl} and C^{m}_{ijkl} are the elastic moduli tensor of the p and m phases respectively, and C^{eff}_{ijkl} is an "effective" modulus. The rationale behind the expression (3.16) is that C^{eff}_{ijkl} represents the "effective" elastic modulus of the macroscopic homogeneous system, and the local (microscopic) perturbations in the elastic moduli about C^{eff}_{ijkl} are described in terms of ΔC_{ijkl}, the difference between the elastic constants of the p and m phases.

In addition, the entire macroscopic system could be subjected to a homogeneous stress state σ^{A}, i.e., the domain Ω behaves as if it is a single homogeneous block in spite of the inhomogeneities at the microscopic scale. Note that σ^{A} should be such that the applied traction on the boundaries of the domain Ω is anti-periodic; i.e., $\sigma \cdot \mathbf{n}$, is opposite on opposite sides of $\partial\Omega$ with $\mathbf{n}$ being the unit normal to the boundary [25, 26].

To obtain the elastic energy, and hence the elastic chemical potential, we have to solve the equation of mechanical equilibrium, namely,

$$\nabla \cdot \sigma^{el} = \frac{\partial \sigma^{el}_{ij}}{\partial r_j} = 0 \quad \text{in } \Omega. \tag{3.18}$$

The Fast Fourier Transform (FFT) based iterative method to solve the above set of partial differential equations is described below.

3.2 The equation of mechanical equilibrium

The elastic moduli and the eigenstrains are periodic on Ω (since they depend on composition field which is periodic on Ω); therefore, the solution to the equilibrium equation (Eqn. (3.18)), should be such that it gives rise to a strain field $\varepsilon(\mathbf{r})$ that is

periodic on Ω (up to an additive constant). The displacement field $\mathbf{u}(\mathbf{r})$ which gives rise to such periodic strain fields can always be written as follows [25]:

$$\mathbf{u} = \mathbf{E} \cdot \mathbf{r} + \mathbf{u}^\star, \tag{3.19}$$

where, $\mathbf{u}^\star$ is a displacement field that is periodic on Ω and $\mathbf{E}$ is a constant, homogeneous strain tensor (assumed to be symmetric without loss of generality, since the antisymmetric part corresponds to a rigid rotation of the cell). It can be shown [25] that $\mathbf{E}$ denotes the mean strain tensor of the cell (See Appendix B):

$$\langle \{\varepsilon_{ij}\} \rangle = E_{ij}, \tag{3.20}$$

with the following definition for the mean of a quantity $\{\cdot\}$:

$$\langle \{\cdot\} \rangle = \frac{1}{V} \int_\Omega \{\cdot\} d\Omega, \tag{3.21}$$

where V is the volume of the representative domain Ω.

If we denote the periodic strain by $\varepsilon^\star$, the strain that we derive from the displacement equation (3.19) becomes (See Appendix B),

$$\varepsilon_{ij} = E_{ij} + \varepsilon^\star_{ij}, \tag{3.22}$$

where,

$$\varepsilon^\star_{ij} = \frac{1}{2} \left\{ \frac{\partial u^\star_i}{\partial r_j} + \frac{\partial u^\star_j}{\partial r_i} \right\}, \tag{3.23}$$

and the equation of mechanical equilibrium (3.18) is

$$\frac{\partial}{\partial r_j} \{ C_{ijkl} (E_{kl} + \varepsilon^\star_{kl} - \varepsilon^0_{kl}) \} = 0. \tag{3.24}$$

Analogous to the expression (3.20) for the homogeneous strain, we can define the mean stress on the domain Ω as follows:

$$\langle \{\sigma^{el}_{ij}\} \rangle = \frac{1}{V} \int_\Omega \sigma^{el}_{ij} d\Omega. \tag{3.25}$$

The mean stress thus calculated should equal the applied stress σ^A [21, 25, 26]. [As a brief aside, we note that while [25,26] used the homogenisation assumption, Jin et al [21] used a variational approach to arrive at the above conclusion, viz., that the mean stress should equal the applied stress.] So, we obtain

$$\sigma^A_{ij} = \frac{1}{V} \int_\Omega C_{ijkl} (E_{kl} + \varepsilon^\star_{kl} - \varepsilon^0_{kl}) d\Omega. \tag{3.26}$$

Further, using the definition (3.21), we can define the following mean quantities:

$$S_{ijkl} = (\langle\{C_{ijkl}\}\rangle)^{-1},\ \langle\{\sigma^{\star}_{ij}\}\rangle = \langle\{C_{ijkl}\varepsilon^{\star}_{kl}\}\rangle,\ \text{and}\ \langle\{\sigma^{0}_{ij}\}\rangle = \langle\{C_{ijkl}\varepsilon^{0}_{kl}\}\rangle. \quad (3.27)$$

Using Eqns. (3.26) and (3.27), we obtain,

$$E_{ij} = S_{ijkl}\ (\sigma^{A}_{kl} + \langle\{\sigma^{0}_{kl}\}\rangle - \langle\{\sigma^{\star}_{kl}\}\rangle). \quad (3.28)$$

Thus, the elasticity problem we wish to solve can be restated as follows:

Given a periodic composition field c on Ω,
solve the **equation of mechanical equilibrium**

$$\frac{\partial}{\partial r_j}\{C_{ijkl}(E_{kl} + \varepsilon^{\star}_{kl} - \varepsilon^{0}_{kl})\} = 0 \text{ on } \Omega, \quad (3.29)$$

with the **constraint**

$$E_{ij} = S_{ijkl}(\sigma^{A}_{kl} + \langle\{\sigma^{0}_{kl}\}\rangle - \langle\{\sigma^{\star}_{kl}\}\rangle) \quad (3.30)$$

and the **boundary condition**

$$\varepsilon^{\star}_{kl} \text{ is periodic on } \Omega. \quad (3.31)$$

As noted in the introduction, Hu and Chen [20] assume an overall zero prescribed strain ($E_{ij} = 0$). In contrast, our present formulation allows for a prescribed overall stress (which is achieved by controlling the strain). This approach is known as "stress-control based on strain-control" (See Appendix D of [26]).

Substituting for C_{ijkl}, and ε^{0}_{kl} in terms of composition, and $\varepsilon^{\star}_{kl}$ in terms of the displacement field in Eqn. (3.29), and using the symmetry properties of the elastic constants and strains, we obtain

$$\frac{\partial}{\partial r_j}\left\{[C^{\text{eff}}_{ijkl} + \alpha(c)\Delta C_{ijkl}]\left(E_{kl} + \frac{\partial u^{\star}_{l}(\mathbf{r})}{\partial r_k} - \varepsilon^{T}\delta_{kl}\beta(c)\right)\right\} = 0. \quad (3.32)$$

$$\left[C^{\text{eff}}_{ijkl}\frac{\partial^2}{\partial r_j \partial r_k} + \Delta C_{ijkl}\frac{\partial}{\partial r_j}\left(\alpha(c)\frac{\partial}{\partial r_k}\right)\right] u^{\star}_{l}(\mathbf{r}) = C^{\text{eff}}_{ijkl}\varepsilon^{T}\delta_{kl}\frac{\partial \beta(c)}{\partial r_j} - \Delta C_{ijkl}E_{kl}\frac{\partial \alpha(c)}{\partial r_j} + \Delta C_{ijkl}\varepsilon^{T}\delta_{kl}\frac{\partial\{\alpha(c)\beta(c)\}}{\partial r_j}. \quad (3.33)$$

3.3 Solution to the equation of mechanical equilibrium

The above equation of mechanical equilibrium (3.33) can be solved using an iterative procedure [20, 26, 77] as shown below.

3.3.1 Zeroth order approximation

Let us assume that $\Delta C_{ijkl} = 0$ to begin with. Then, the equation of mechanical equilibrium (3.18) reduces to

$$C^{\text{eff}}_{ijkl}\frac{\partial^2 u^\star_l(\mathbf{r})}{\partial r_j \partial r_k} = C^{\text{eff}}_{ijkl}\varepsilon^T \delta_{kl}\frac{\partial \beta(c)}{\partial r_j}. \tag{3.34}$$

Taking $\sigma^T_{ij} = C^{\text{eff}}_{ijkl}\varepsilon^T\delta_{kl}$,

$$C^{\text{eff}}_{ijkl}\frac{\partial^2 u^\star_l(\mathbf{r})}{\partial r_j \partial r_k} = \sigma^T_{ij}\frac{\partial \beta(c)}{\partial r_j}. \tag{3.35}$$

The above equation can be solved in the Fourier space (See Appendix C). Defining G^{-1}_{il} as $C_{ijkl}g_j g_k$ (where $\mathbf{g}$ is the vector in the Fourier space), we can write the solution (in the Fourier space) as follows:

$$\left\{(u^\star_l)^0\right\}_{\mathbf{g}} = -JG_{il}\sigma^T_{ij}g_j\{\beta(c)\}_{\mathbf{g}}, \tag{3.36}$$

where the superscript on $u^\star_k$ denotes the order of approximation, and J is $\sqrt{(-1)}$.

3.3.2 Higher order approximations

Having the zeroth order approximation it is possible to refine the solution (See Appendix C). We can write the nth order refined solution using the $(n-1)$th order solution as follows:

$$\{(u^\star_l)^n\}_{\mathbf{g}} = -JG_{il}\Lambda^{n-1}_{ij}g_j, \tag{3.37}$$

where

$$\begin{aligned}\Lambda^{n-1}_{ij} &= \sigma^T_{ij}\{\beta(c)\}_{\mathbf{g}} - \Delta C_{ijmn}E^{n-1}_{mn}\{\alpha(c)\}_{\mathbf{g}} \\ &\quad +\Delta C_{ijmn}\varepsilon^T\delta_{mn}\{\alpha[c(\mathbf{r})]\ \beta[c(\mathbf{r})]\}_{\mathbf{g}} - \Delta C_{ijmn}\left\{\alpha[c(\mathbf{r})]\frac{\partial (u^\star_m)^{n-1}(\mathbf{r})}{\partial r_n}\right\}_{\mathbf{g}}\end{aligned} \tag{3.38}$$

3.4 Elastic energy and the corresponding chemical potential

Let the elastic strain energy be given by

$$E_{el} = \int_{\Omega} e_{el}(\mathbf{r}) d\mathbf{r}, \tag{3.39}$$

where, the local elastic energy density e_{el} is given by

$$e_{el}(\mathbf{r}) = \frac{1}{2} C_{ijkl} \varepsilon^{el}_{ij} \varepsilon^{el}_{kl}. \tag{3.40}$$

Since

$$\varepsilon^{el}_{ij} = \varepsilon_{ij} - \varepsilon^{o}_{ij}, \tag{3.41}$$

and,

$$\varepsilon_{ij} = E_{ij} + \varepsilon^{\star}_{ij}, \tag{3.42}$$

we obtain,

$$e_{el}(\mathbf{r}) = \frac{1}{2} C_{ijkl} (E_{ij} + \varepsilon^{\star}_{ij} - \varepsilon^{0}_{ij})(E_{kl} + \varepsilon^{\star}_{kl} - \varepsilon^{0}_{kl}) \tag{3.43}$$

From the above expressions and the definition of μ^{el}, the elastic chemical potential (3.7), we obtain

$$\begin{aligned} N_V \mu^{el} &= \frac{1}{2} \alpha'(c) \Delta C_{ijkl} (E_{ij} + \varepsilon^{\star}_{ij} - \varepsilon^{0}_{ij})(E_{kl} + \varepsilon^{\star}_{kl} - \varepsilon^{0}_{kl}) \\ &\quad - \beta'(c) \varepsilon^{T} \delta_{ij} C_{ijkl} (E_{kl} + \varepsilon^{\star}_{kl} - \varepsilon^{0}_{kl}), \end{aligned} \tag{3.44}$$

where, the prime represents the differentiation with respect to c. Note that the above expression is the same as that given by equation 18 in [18].

To summarise, the CH equation that we wish to solve is Eqn. (3.5), namely,

$$\frac{\partial c}{\partial t} = \nabla \cdot M \nabla (\mu^{ch} + \mu^{el}). \tag{3.45}$$

The μ^{ch} is given by (3.10), namely,

$$\mu^{ch} = h_f(c) - 2\kappa \nabla^2 c, \tag{3.46}$$

with, $h_f(c) = (\partial f_0 / \partial c) = 2A_b c(1-c)(1-2c)$. The μ^{el} is given by Eqn. (3.44), namely,

$$\begin{aligned} N_V \mu^{el} &= \frac{1}{2} \alpha'(c) \Delta C_{ijkl} (E_{ij} + \varepsilon^{\star}_{ij} - \varepsilon^{0}_{ij})(E_{kl} + \varepsilon^{\star}_{kl} - \varepsilon^{0}_{kl}) \\ &\quad - \beta'(c) \varepsilon^{T} \delta_{ij} C_{ijkl} (E_{kl} + \varepsilon^{\star}_{kl} - \varepsilon^{0}_{kl}), \end{aligned} \tag{3.47}$$

3.5 Non-dimensionalisation

All the parameters used in our simulations are non-dimensional. We carry out the non-dimensionalisation using the characteristic length L', energy E', and time T' given below (where, the prime represents the fact that these quantities are dimensional):

$$L' = \left(\frac{\kappa'}{A'_b}\right)^{\frac{1}{2}}, \tag{3.48}$$

$$E' = A'_b, \tag{3.49}$$

$$T' = \frac{L'^2(c'_p - c'_m)^2}{M'E'}. \tag{3.50}$$

The details of the non-dimensionalisation are shown in Appendix A; we note here that our choice of non-dimensionalisation renders κ, A_b, and M unity. Thus, the non-dimensional Cahn-Hilliard equation is given as

$$\frac{\partial c}{\partial t} = \nabla^2(h - 2\nabla^2 c + \mu^{el}), \tag{3.51}$$

where, the non-dimensional μ^{el} is obtained by using a scaled non-dimensional C^*_{ijkl} as follows: $C^*_{ijkl} = C_{ijkl}/N_V$. Finally, our non-dimensional time and length units correspond to 0.02 seconds and 1 nano-metre, respectively (as we show in the Appendix A).

3.6 Numerical implementation

3.6.1 Fourier transform and discretisation

Let us consider the domain Ω of size $L_x \times L_y \times L_z$; let it be discretised with nodes at distances Δx, Δy, and Δz along the x, y, and z axes, respectively, and let N_x, N_y, and N_z be the number of nodes along x, y, and z axes, respectively. Thus, any node on the domain is identified by a set of integers, namely, (i, j, k) (and by a pair of integers (i, j) in 2D). We define the (discrete) Fourier transform ($\mathcal{F}$) of a function

$H(\mathbf{r})$, where $\mathbf{r}$ is the real-space Cartesian vector, as follows:

$$\begin{aligned}\mathcal{F}(H(\mathbf{r})) = H(\mathbf{g}) &= \sum_{\Omega} H(\mathbf{r}) \exp\left(-2\pi J \mathbf{g}' \cdot \mathbf{r}\right) d\mathbf{r} \\ &= \sum_{i=1}^{N_x} \sum_{j=1}^{N_y} \sum_{k=1}^{N_z} H(\mathbf{r}) \exp\left(-J\mathbf{g} \cdot \mathbf{r}\right) d\mathbf{r}, \end{aligned} \tag{3.52}$$

where, $\mathbf{g}'$ is the reciprocal space vector, $\mathbf{g} = 2\pi\mathbf{g}'$ and $J = \sqrt{(-1)}$. Similarly, the inverse Fourier transform is defined as follows:

$$\begin{aligned}\mathcal{F}^{-1}(H(\mathbf{g})) = H(\mathbf{r}) &= \sum_{\Omega} H(\mathbf{g}) \exp\left(2\pi J \mathbf{g}' \cdot \mathbf{r}\right) d\mathbf{g} \\ &= \sum_{i=1}^{N_x} \sum_{j=1}^{N_y} \sum_{k=1}^{N_z} H(\mathbf{g}) \exp\left(J\mathbf{g} \cdot \mathbf{r}\right) d\mathbf{g}. \end{aligned} \tag{3.53}$$

The reciprocal vector $\mathbf{g}$ is given as follows: $\mathbf{g} = m_1\mathbf{g_1} + m_2\mathbf{g_2} + m_3\mathbf{g_3}$, where, m_i are integers, and $\mathbf{g_1}$, $\mathbf{g_2}$, and $\mathbf{g_3}$ are the basis vectors of the reciprocal lattice:

$$\mathbf{g_1} = 2\pi \frac{L_y\hat{y} \times L_z\hat{z}}{L_x\hat{x} \cdot L_y\hat{y} \times L_z\hat{z}}; \tag{3.54}$$

$$\mathbf{g_2} = 2\pi \frac{L_z\hat{z} \times L_x\hat{x}}{L_x\hat{x} \cdot L_y\hat{y} \times L_z\hat{z}}; \tag{3.55}$$

and,

$$\mathbf{g_3} = 2\pi \frac{L_x\hat{x} \times L_y\hat{y}}{L_x\hat{x} \cdot L_y\hat{y} \times L_z\hat{z}}. \tag{3.56}$$

Let us consider the equation (3.51) and take the (spatial-) Fourier transform on both sides of the equations (with the notation that $\{(\cdot)\}_{\mathbf{g}}$ is the Fourier transform of $(\cdot)$):

$$\frac{\partial\{c\}_{\mathbf{g}}}{\partial t} = -g^2(\{h_f\}_{\mathbf{g}} + 2g^2\{c\}_{\mathbf{g}} + \{\mu^{el}\}_{\mathbf{g}}). \tag{3.57}$$

Note that these equations are written for every node $\mathbf{g}$ on the reciprocal lattice.

The semi-implicit discretisation of the above equation is then obtained as follows [78]:

$$\frac{c(\mathbf{g}, t+\Delta t) - c(\mathbf{g}, t)}{\Delta t} = -g^2\{h_f\}_{\mathbf{g}} - 2g^4 c(\mathbf{g}, t+\Delta t) - g^2\{\mu^{el}\}_{\mathbf{g}}. \tag{3.58}$$

$$c(\mathbf{g}, t+\Delta t) = \frac{c(\mathbf{g}, t) - g^2\Delta t(\{h_f\}_{\mathbf{g}} + \{\mu^{el}\}_{\mathbf{g}})}{1 + 2\Delta t g^4}, \tag{3.59}$$

where Δt is the time step for the numerical integration. Thus the problem of microstructural evolution reduces to numerically solving the discretised equation(s) above.

All our simulations in this thesis are carried out on a (discretised) 2D domain. Usually, in these simulations, the equation of mechanical equilibrium is solved in 3D under a plane strain assumption. However, in this thesis, we solve the equation of mechanical equilibrium in 2D. In such case, the real space is discretised with nodes at distances Δx along the x-axis and nodes at distances Δy along the y-axis, and the reciprocal lattice vectors are given by $\mathbf{g_1} = (2\pi/L_x)\,\hat{x}$ and $\mathbf{g_2} = (2\pi/L_y)\,\hat{y}$.

The (discrete) Fourier transforms needed for our calculations have been carried out using the free software FFTW (Fastest Fourier Transform in the West) developed by Frigo and Johnson [79].

3.6.2 Algorithm for microstructural evolution

The following is the algorithm for microstructural evolution:

1. Given a composition profile at time t, we calculate the μ^{ch} (using Eqn. (3.46)) and its Fourier transform.

2. We solve the problem of mechanical equilibrium for the given composition distribution, thereby obtaining μ^{el} (using Eqn. (3.47)) and its Fourier transform. While solving the equation of mechanical equilibrium, according to our formulation described above, at each time step, we need to

   (a) get the zeroth order solution (using Eqn. (3.36)), and

   (b) refine the zeroth order solution (using Eqn. (3.37)) till the error in displacements is less than a given value (typically, less than 10^{-8} in the following simulations). We use the L^2 norm in defining the error: Let $\mathbf{u}^n(i,j)$ and $\mathbf{u}^{n+1}(i,j)$ be the displacement solutions at the grid point (i,j). Let the total number of grid points in the x and y-directions be M and N respectively. Then, the error is

$$\text{Error} = \left[\sum_{i=1}^{M}\sum_{j=1}^{N}(\mathbf{u}^{n+1}(i,j) - \mathbf{u}^{n}(i,j)) \cdot (\mathbf{u}^{n+1}(i,j) - \mathbf{u}^{n}(i,j))\right]^{\frac{1}{2}}. \tag{3.60}$$

Since this is an iterative method, it is possible to use the displacements from the previous time step as the starting point and thus expedite the iterative refinement procedure. Hence, in our implementation, from the second time step onwards, the solution from the previous step is used as the starting point for refinement of the solution.

3. Using $\{\mu^{ch}\}_{\mathbf{g}}$ and $\{\mu^{el}\}_{\mathbf{g}}$ in Eqn. (3.59), we calculate the composition profile at some future time $t + \Delta t$.

4. We repeat steps 1-3 to march in time for the given number of time steps.

3.6.3 A note on interpolation functions $\alpha(c)$ and $\beta(c)$

The function used for eigenstrain interpolation $\beta(c)$ (see Eqn. (3.15)) in our model depends on the reference state for the measurement of the eigenstrain. If the strain-free matrix phase is used as the reference state, then $\beta(c_m) = 0.0$ and $\beta(c_p) = 1.0$. If the average alloy of composition c_0 is used as the reference state, then $\beta(c_m) = -c_0$ and $\beta(c_p) = 1.0 - c_0$. The above conditions are only on the value of β for the m and p phases, and hence, we have the freedom to choose any functional form for the intermediate values.

Similar to β, there are several ways of defining the interpolating function $\alpha(c)$ in Eqn. (3.16). However, if ΔC_{ijkl} is given by (3.17), then, the definition of α is determined by the expression for the "effective" elastic modulus. In Table 3.1 we summarise some definitions of "effective" moduli used in the present study (and some other studies in the literature as well), and the corresponding α expression.

We note that the calculation of α and β functions as well as their derivatives with respect to the composition variable involves tanh and such other costly function calls. In our numerical implementation, we have tabulated α and β and read them off the tables during the calculations. Each table typically consists of 140000 entries and tabulates these functions for composition values ranging from -0.2 to 1.2.

Sl.no	Expression for α	Expression for C^{eff}_{ijkl}
1	$\left\{\frac{1}{2}(\tanh(2ac-a))\right\}-\frac{1}{2}$, a, a constant	$\frac{1}{2}(C^p_{ijkl}+C^m_{ijkl})$ (See [26])
2	$\{c^3(10-15c+6c^2)\}-\frac{1}{2}$ (See [80])	$\frac{1}{2}(C^p_{ijkl}+C^m_{ijkl})$
3	c	C^m_{ijkl} (See [18])
4	$c-1$	C^p_{ijkl}
5	$c-c_0$	$C^{\text{eff}}=(1-c_0)C^m+c_0C^p$ (See [20])

Table 3.1: The interpolation function α and the corresponding C^{eff}_{ijkl}

3.7 Comparison with analytical solutions

As noted earlier, we have the freedom to choose from a variety of interpolation functions α and β. In this chapter, we wish to compare our numerical results with corresponding sharp interface, analytical results. The latter results are obtained by attributing the eigenstrain to the precipitate phase, using the strain-free matrix as the reference state. Thus, the tanh function and the function of Wang et al [80] are suitable for our studies.

In particular, the function of Wang et al is ideal for our purposes since it approaches zero and unity smoothly when the composition goes to zero and unity; hence, in all our calculations below, we have used the following interpolation functions:

$$\beta(c) = c^3(10 - 15c + 6c^2), \tag{3.61}$$

and,

$$\alpha(c) = \{c^3(10 - 15c + 6c^2)\} - \frac{1}{2}. \tag{3.62}$$

In addition to β, the complete prescription of eigenstrain includes the tensor $\varepsilon^T \delta_{ij}$, where ε^T is the strength of the eigenstrain, and δ_{ij} is the Kronecker delta; hence (as noted earlier), the eigenstrain ε^0 is dilatational. In all our calculations, we use a value of $\varepsilon^T = 0.01$ for the precipitate phase, and $\varepsilon^T = 0.0$ for the cavity.

For a system with cubic elastic constants, the circular averages of the Voigt constants ($\overline{C}_{11}$, $\overline{C}_{12}$, and $\overline{C}_{44}$) can be related to the average shear modulus G, the Poisson's ratio ν, and the anisotropy parameter A_Z [55] using the following expressions:

$$G = \overline{C}_{44}, \tag{3.63}$$

$$\nu = \frac{1}{2}\frac{\overline{C}_{12}}{\overline{C}_{12} + \overline{C}_{44}}, \tag{3.64}$$

and,

$$A_Z = \frac{2\overline{C}_{44}}{\overline{C}_{11} - \overline{C}_{12}}. \tag{3.65}$$

If A_Z, the anisotropy parameter is equal to unity, the elastic constants are isotropic. If it is greater (less) than unity, then the elastic constants have a cubic anisotropy, with $\langle 10 \rangle$ directions ($\langle 11 \rangle$ directions) being the softest [81, 82]. Further, we define the inhomogeneity ratio δ as the ratio of the shear modulus of the precipitate to

that of the matrix: $\delta = \overline{C}^p_{44}/\overline{C}^m_{44}$. If δ is equal to unity, then the system is elastically homogeneous. If it is greater or less than unity, then the precipitate is harder or softer than the matrix, respectively.

In all our calculations, we maintain the Poisson's ratio, and the anisotropy parameter to be the same for both the matrix and precipitate phases. Thus, prescribing ν, A_Z, and, G of one of the phases, say, the matrix phase, and the inhomogeneity parameter δ, is sufficient to completely characterise the elastic moduli used in the calculations. In all our calculations, we keep the shear modulus of the matrix (G^m) fixed at 400 and the Poisson's ratio (ν) at 0.3.

In Table 3.2, we list all the parameters used in our simulations; these include the discretisation and numerical simulation related parameters (Δx, Δy, Δt, and, the allowed error in the displacement solution), the kinetic parameter (M), the chemical free energy related parameters (A_b, and κ), and the elastic parameters that do not vary across simulations (G^m, ν, and ε^T).

In all the calculations described in this chapter, the precipitates are placed at the centre of the domain: this is achieved by calculating the distance of any grid point from the centre, and making the composition of the grid point unity if it lies within the precipitate, and zero, otherwise. Hence, the precipitate-matrix interface is jagged in all the simulations.

3.7.1 Circular and elliptic precipitates

The analytical solutions are obtained for a single (circular or elliptic) precipitate in an infinite matrix [28, 83]. We use periodic boundary conditions in our numerical calculations; by making the volume fraction of the precipitate as small as our simulation allows, we can approach this limit of a single precipitate in an infinite matrix. In the present set of calculations, we use a precipitate radius R of 25, while the simulation cell size $L_x = L_y = 512$: thus the volume fraction of the precipitate is ≈ 0.0075. In the case of non-circular precipitates, R is the equivalent radius: $R = \sqrt{(a_p/\pi)}$, where a_p is the area of the precipitate. We have used a grid of $\Delta x = 1$ and $\Delta y = 1$; and a tolerance value of 10^{-8} for the convergence of the displacement

Parameter type	Parameter	Value used
Cahn-Hilliard Model	M	1.0
	κ	1.0
	A_b	1.0
Elastic	G^m	400.0
	ν	0.3
	ε^T	0.01 (for precipitates)
		0.0 (for cavities)
Simulation	Δx	1.0
	Δy	1.0
	Δt	1.0
	Allowed error in displacements	less than 10^{-8}

Table 3.2: Parameters used in the simulations

solutions.

In Figures 3.4 and 3.5 we compare the numerical solutions for the principal and shear stress components as a function of distance from the centre of the circular precipitate. The corresponding analytical solutions are also shown (as a dotted line) for a direct comparison. The stress components (normalised by the characteristic stress $G^m\varepsilon^T$) are plotted against the normalised distance (r/R) from the centre of the precipitate along the x-axis. The elastic constants are isotropic (i.e., $A_Z = 1$), and, the precipitate is softer than the matrix ($\delta = 0.5$).

From the analytical results, we know that σ_{xx} is continuous and σ_{yy} is discontinuous across the p-m interface; σ_{xy} is zero everywhere along the x-axis.

From these figures, it is clear that the numerical solutions agree well with the analytical ones except in the vicinity of the interface. Further, the width of the region over which there is significant difference can be decreased by reducing the grid size. This is due to the difficulty in capturing discontinuities and sharp changes using Fourier series expansions. As is well known, this effect, known as the Gibbs phenomenon, never disappears even in the limit of an infinite number of terms; as more terms are included, the location of the overshoot moves closer to the discontinuity (See p. 333 of [84]). In addition, the stress at the edge of the simulation cell is very nearly zero, indicating that the matrix is effectively infinite.

We have carried out similar comparisons of our numerical solutions for the strain components at the centre of elastically isotropic (circular and elliptic), soft ($\delta = 0.5$), homogeneous ($\delta = 1.0$), and hard ($\delta = 2.0$) precipitates, as well as for solutions inside a circular and an elliptic homogeneous precipitate when the elastic constants are anisotropic (with $A_Z = 3.0$) (with the corresponding analytical solutions given by Mura (p. 142 of [28]). We define the normalised error in the principal strain components at the centre of the precipitate as follows:

$$\text{Normalised Error} = \frac{\varepsilon^{\text{Numerical}} - \varepsilon^{\text{Analytical}}}{\varepsilon^T} \tag{3.66}$$

In all the calculations, we find that the normalised error is 0.8% or less (for a volume fraction of ≈ 0.0075). The shear strain components at the centre of the precipitates are identically zero for all these cases: in our numerical calculations also we find

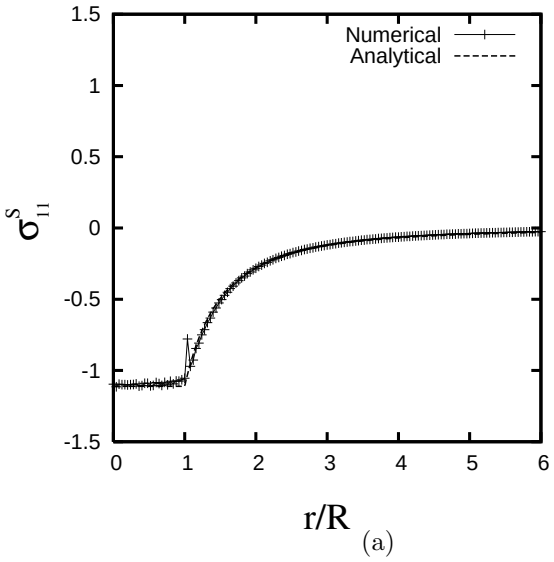

(a)

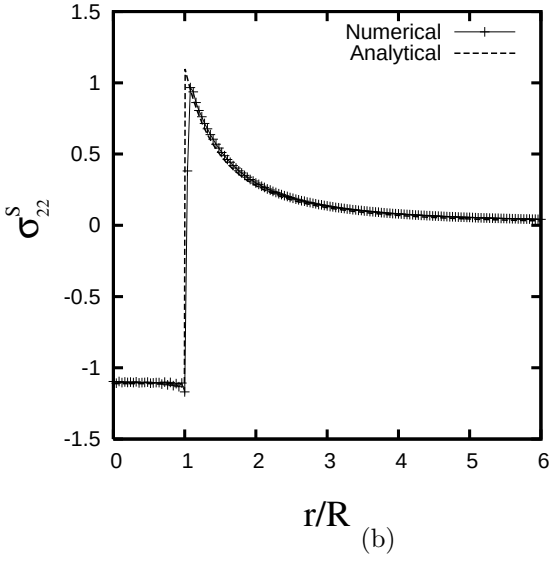

(b)

Figure 3.4: The normalised principal stress components (a) σ^s_{11}, and (b) σ^s_{22} as a function of normalised distance: analytical and numerical solutions along the x-axis (from the centre of a circular precipitate). The distance is normalised by R, the precipitate radius, while the stress is normalised by the characteristic stress $G^m\varepsilon^T$. The line through the data points is drawn only as a guide to the eye. $R = 25$; $L_x = L_y = 512$; $\delta = 0.5$; $A_Z = 1$.

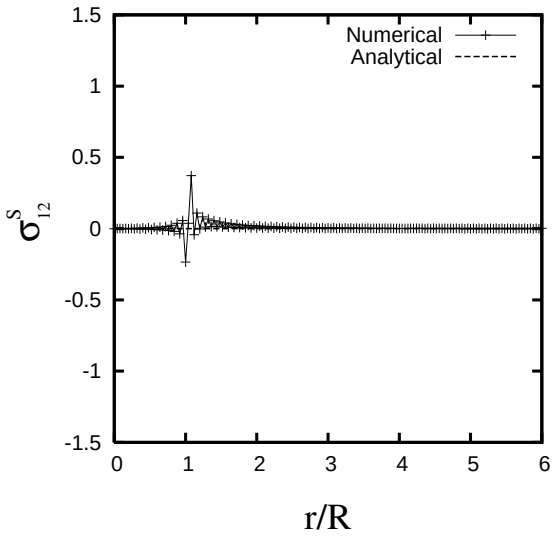

Figure 3.5: The normalised shear stress component σ^s_{12} as a function of normalised distance: analytical and numerical solutions along the x-axis (from the centre of a circular precipitate). The distance is normalised by R, the precipitate radius, while the stress is normalised by the characteristic stress $G^m\varepsilon^T$. The line through the data points is drawn only as a guide to the eye. $R = 25$; $L_x = L_y = 512$; $\delta = 0.5$; $A_Z = 1$.

that the shear strain components are of the order of 10^{-5} or less.

3.7.2 Cavity under an externally applied stress

It is generally believed that iterative procedures like the one described here are not suitable when the inhomogeneity ratio is very high [19, 24]. There are also reports suggesting that there is a linear relationship between the inhomogeneity and the number of iterations needed to reach the solution [26]. However, in our calculations, for a circular cavity in a plate under an uniaxial applied stress, we are able to obtain the solution with 9 iterations. The solution obtained is shown in Figure 3.6. In these cases, the inhomogeneity (δ) is 10^{-8}. Thus, obtaining the solutions in 9 iterations is both surprising, and highly encouraging.

Our numerical solutions also agree well with the analytical solutions (See page 91 of [85]). In Figure 3.7, we plot the number of iterations required for any given inhomogeneity. We see that beyond $\delta = 0.01$, the number of iterations remains a

constant at 9. We further note that the number of iterations is also sensitive to the volume fraction of the cavity; as the volume fraction of the cavity increases, the number of iterations needed to reach the solution increases. However, the earlier conclusion is still valid, viz., for a given volume fraction, the number of iterations needed to reach the solution becomes a constant beyond some specific inhomogeneity value.

3.8 Characterisation of the numerical method: accuracy of the elastic solution

The accuracy with which we solve the equation of mechanical equilibrium depends on the refinement of the grid as well as the tolerance within which the displacement solution is obtained. Further, as noted earlier, the numerical solutions approach the analytical solution only in the limit of the volume fraction of the precipitate approaching zero. In this subsection, we describe the effect of all these three parameters on the accuracy of the elastic solution. In all the cases below, the precipitates are circular ($R = 50$, $L_x = L_y = 1024$ so that the volume fraction is about 0.0075) and are elastically isotropic ($A_Z = 1$): the normalised error in the principal components of strain at the centre of the precipitate (see Eqn. (3.66)) is used as a measure of accuracy.

3.8.1 Effect of grid refinement

In Figure 3.8, we summarise the effect of grid refinement on the solution for both hard ($\delta = 2.0$) and soft ($\delta = 0.5$) precipitates. The coarsest grid $\Delta x = 2$ that we have used, produced the largest (normalised) error of less than 1.4% in the principal strain at the centre of the precipitate. Further, refining the grid to less than $\Delta x = 1$ did not increase the accuracy much. In all our calculations in this thesis, we use a grid size of unity.

The relatively large error in the case where the grid is $\Delta x = 2$ (though small in itself) as compared to the case where $\Delta x = 1$, could be due to the jagged nature

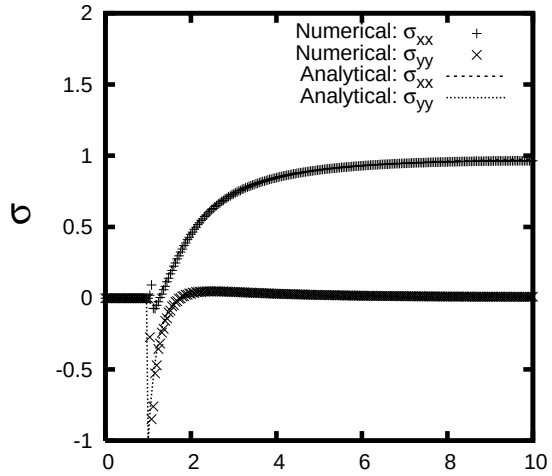

(a)

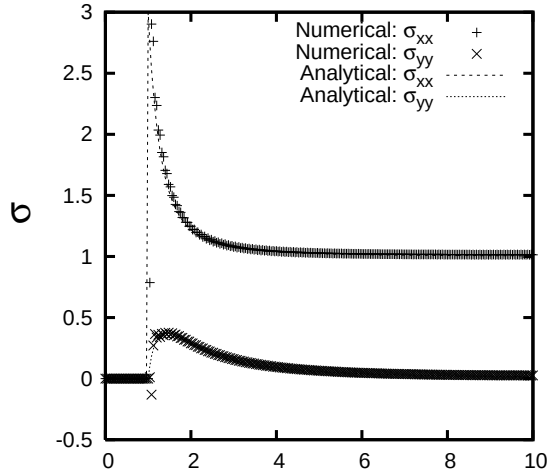

(b)

Figure 3.6: The σ_{xx} and σ_{yy} stress components along the (a) x-axis and (b) y-axis from the centre of a circular cavity in a square domain under an applied tensile stress along the x-axis. $R = 25$; $L_x = L_y = 512$; $\sigma^A = 1$; $\delta = 10^{-8}$; $\varepsilon^T = 0$.

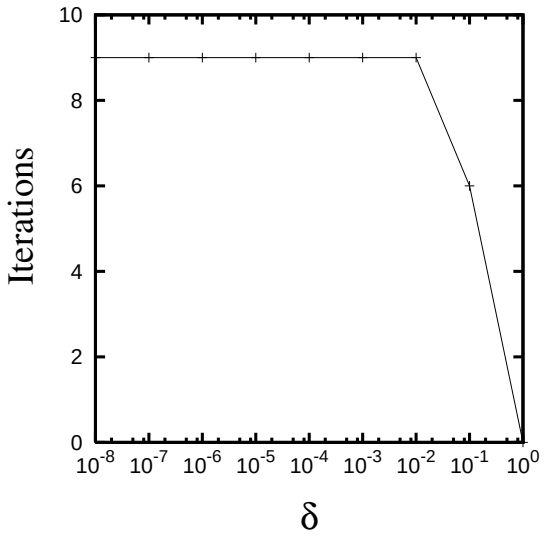

Figure 3.7: The effect of inhomogeneity on convergence; data from simulations of a circular cavity in a square domain under an externally applied uniaxial stress (Figure 3.6). The line through the data points is drawn only as a guide to the eye.

of the interface. An increase in the grid size, or the size of the precipitate leads to a less jagged interface (which approximates the actual shape better) resulting in a reduction of the error.

3.8.2 Tolerance for the error in displacement solution

The equation of mechanical equilibrium is solved using an iterative procedure, by refining the displacement solution within a given tolerance value: we use spectral differentiation to obtain the strains from these displacement values. In Figure 3.9 (a), we indicate the effect of the tolerance value on the accuracy of the elastic (strain) solution (for both soft ($\delta = 0.5$) and hard ($\delta = 2$) precipitates). As is clear from the figure, refining the displacement solution beyond 10^{-8}, does not refine the solution much, while the further refinement only increases the required number of iterations (See Figure 3.9 (b)). We set the tolerance limit in our calculations at 10^{-8}.

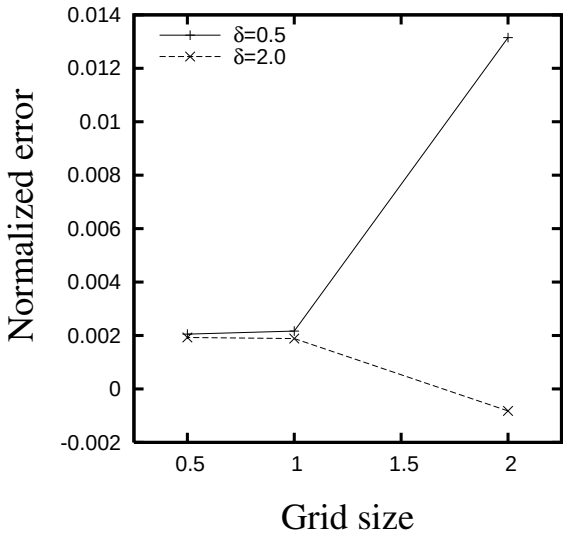

Figure 3.8: The normalised error in the principal strain component at the centre of a circular precipitate as a function of the grid size. The strain is normalised by the strength of the eigenstrain $\varepsilon^T = 0.01$ (see Eqn. (3.66)). The lines through the data points are drawn only as a guide to the eye. $R = 50; L_x = L_y = 1024;\ A_Z = 1$.

3.8.3 Effective moduli definition

The definition used for the "effective moduli" (with which we calculate the zeroth order solution) has a strong effect on the convergence properties. In Table 3.3, we list the number of iterations needed to converge to the solution in three different cases, viz., $\frac{1}{2}(C^m_{ijkl}+C^p_{ijkl})$, C^m_{ijkl} and C^p_{ijkl}. Even though all the three expressions lead to the same solution, using C^m_{ijkl} or C^p_{ijkl} as the effective modulus takes two to five times the number of iterations as compared to the case when the arithmetic average of the elastic constants is used as the effective modulus; further, when we use the arithmetic average, the number of iterations needed for convergence is independent of δ. This is quite surprising because the volume fraction of the precipitate is quite small (≈ 0.0075); at present, the reason for the faster convergence on using the arithmetic average of the moduli as C^{eff} is not clear to us.

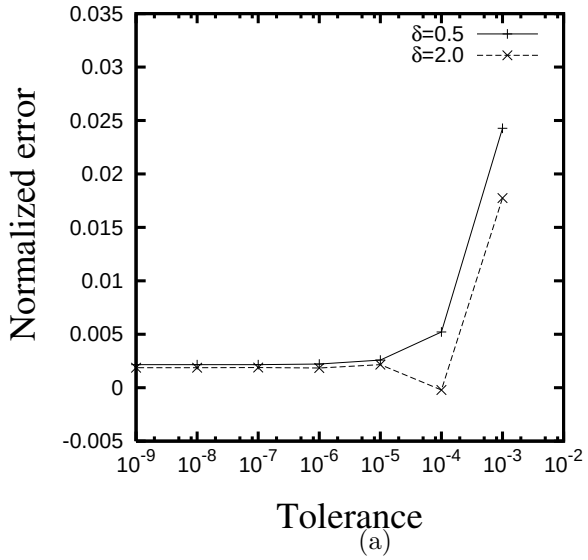

(a)

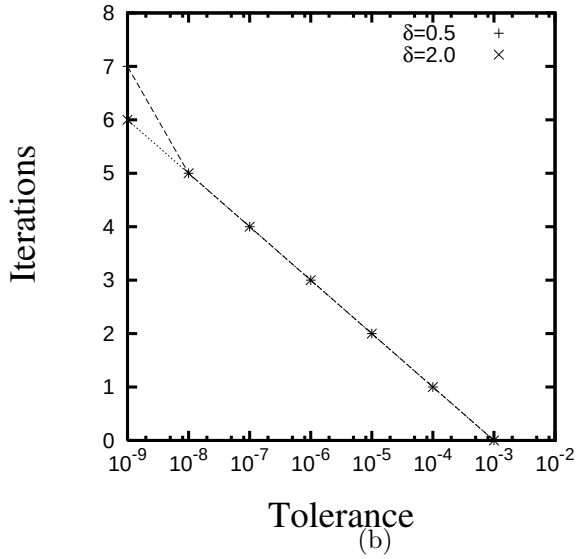

(b)

Figure 3.9: (a) The normalised error in the principal strain component at the centre of a circular precipitate as a function of the tolerance value for the refinement of the displacement solution. The strain is normalised by the strength of the eigenstrain $\varepsilon^T = 0.01$. The lines through the data points are drawn only as a guide to the eye. (b) The increase in the number of iterations with the decrease in the tolerance for the refinement of the displacement solution. The lines through the data points are drawn only as a guide to the eye.

Inhomogeneity	Expression for C_{ijkl}^{eff}	Number of iterations
Hard precipitate ($\delta = 2.0$)	$\frac{1}{2}(C_{ijkl}^{p} + C_{ijkl}^{m})$	4
	C_{ijkl}^{m}	22
	C_{ijkl}^{p}	4
Soft precipitate ($\delta = 0.5$)	$\frac{1}{2}(C_{ijkl}^{p} + C_{ijkl}^{m})$	4
	C_{ijkl}^{m}	7
	C_{ijkl}^{p}	8

Table 3.3: The effect of interpolation function α and the corresponding C_{ijkl}^{eff} on convergence.

3.9 Homogenised quantities

In Section 3.7 above, we compared our numerical results with the available analytical sharp interface solutions. Though there are no exact analytical solutions for obtaining homogenised quantities (say, homogenised strain and homogeneous moduli) in an elastically inhomogeneous system, some approximate solutions and trends are known for simple system geometries. In this section, we describe our results from a numerical calculation of homogeneous strain and homogeneous moduli, with relevant comparisons with (approximate) analytical solutions. Further, we also indicate that the contribution of homogeneous strain to the total elastic energy could be considerable, and hence is important for an accurate study of microstructural evolution in elastically inhomogeneous solids.

3.9.1 Homogeneous strain

In Figure 3.10 (a), we summarise the effect of volume fraction of the precipitate on the accuracy of the elastic solution: we plot the value of the homogeneous strain normalised by the strength of the eigenstrain ε^T as a function of volume fraction for soft ($\delta = 0.5$), homogeneous ($\delta = 1.0$) and hard precipitates ($\delta = 2.0$). In the case of the homogeneous precipitate the normalised homogeneous strain equals the volume fraction of the precipitate; this is in agreement with the analytical result (See p.206 of [29]). In the case of a hard (soft) precipitate in a soft (hard) matrix, the homogeneous strain is greater (smaller) than the volume fraction of the precipitate as expected. Further, as the volume fraction of the precipitate tends to zero, the homogeneous strain also tends to zero.

In Figure 3.10 (b), we show that the (normalised) difference in the elastic energy, namely, the difference between the energy of the system with prescribed zero displacement at the boundary and that with zero tractions on the boundary. The normalisation was carried out using the elastic energy of the system with prescribed tractions at the boundary. As is clear from the figure, even at a volume fraction of 0.2, the energies differ by 100% and for a volume fraction of 0.5, the energy difference could be as large as 500%. Hence, not calculating the homogeneous strain

while solving the equation of mechanical equilibrium (as done by Leo et al [18]), or imposing the zero displacement constraint on the boundary while the natural boundary conditions demand zero traction at the boundary (as done by Hu and Chen [20], for example) could produce erroneous results.

3.9.2 Homogeneous moduli

We now consider a square domain of the matrix with a circular precipitate at its centre. Let both the precipitate and the matrix be isotropic (with Poisson's ratio of 0.3). Let a tensile stress of a given magnitude (unity, in this case) be applied. The effective shear modulus of the composite can then be obtained by assuming isotropic elasticity and calculating the Young's modulus and Poisson's ratio using the tensile and lateral homogeneous strains.

In Figure 3.11 (a), we show the normalised homogeneous shear modulus (G^{hom}/G^m) thus obtained for a composite with soft (δ=0.2) and hard (δ=5) precipitates. For comparison, we also plot the analytical solutions for the dilute distribution of precipitates with prescribed stress (DD-Σ) and prescribed strain (DD-E) for the same δ values obtained using the expressions (8.2.13 b) and (8.2.14 b), respectively of Nemat-Nasser and Hori [30]; our numerical results are in good agreement with the DD-Σ solutions, especially at smaller volume fractions. Similarly, our numerical calculations of the normalised homogeneous shear moduli of a 2D composite consisting of circular holes (see Figure 3.11 (b)) are also in good agreement with the corresponding DD-Σ analytical solutions described by the expression (5.1.15 a) in [30].

3.10 Summary

In this chapter, we have presented a phase field model which incorporates the elastic solutions obtained by solving the equation of mechanical equilibrium in an elastically inhomogeneous system. The equation of mechanical equilibrium is solved both under prescribed traction and displacement boundary conditions; further, we show that

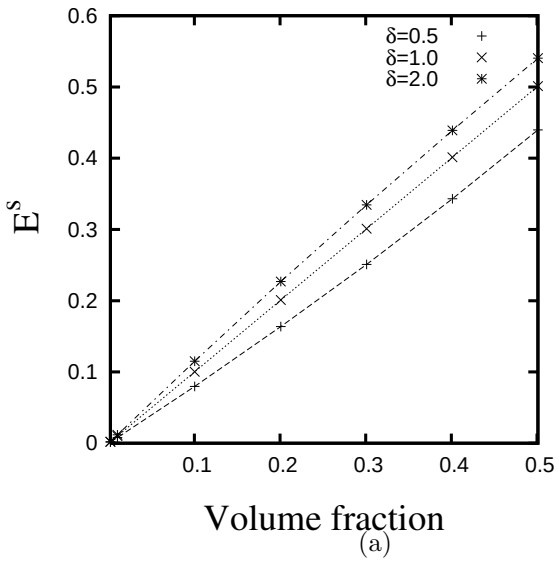

(a)

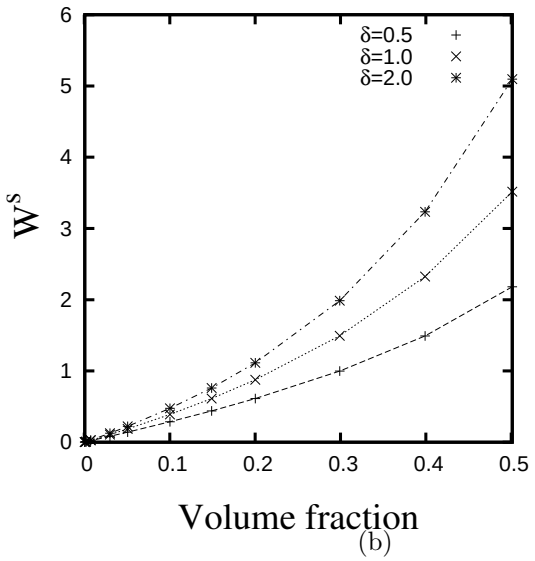

(b)

Figure 3.10: The (a) normalised homogeneous strain and (b) the normalised difference in the elastic energy as a function of the volume fraction of the precipitate. The homogeneous strain is normalised by the strength of the eigenstrain $\varepsilon^T = 0.01$, while, the elastic energy was normalised by the elastic energy for an unconstrained system. The lines through the data points are drawn only as a guide to the eye.

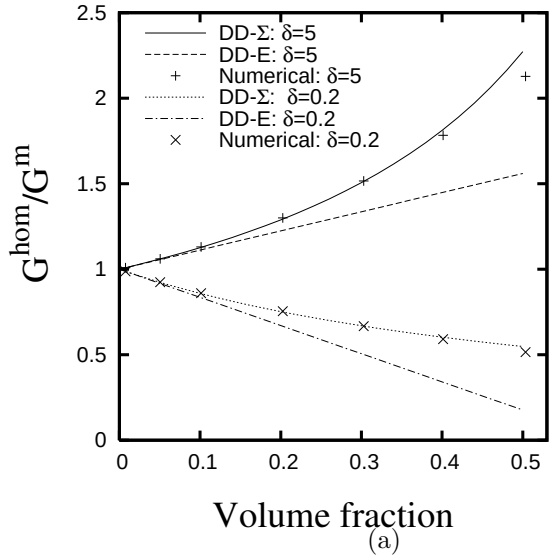

(a)

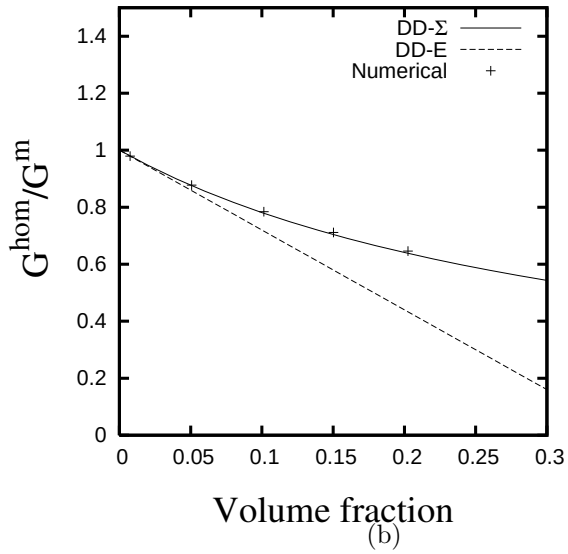

(b)

Figure 3.11: The normalised effective shear modulus for (a) soft (δ=0.2) and hard (δ=5) inhomogeneities, and (b) cavities.

our iterative procedure is both accurate and efficient. Finally, we characterise our numerical method, and show that our elastic solutions agree very well with the corresponding analytical solutions. In the following chapters, we use our phase field model to study microstructural evolution in two systems where elastic inhomogeneity plays a key role, namely, rafting in systems with dilatational misfit (Chapter **??**) and phase inversion (Chapter **??**).

Appendix A

Non-dimensionalisation

In this section, all the primed quantities are dimensional; as noted in Chapter 3, we use the characteristic energy E', time T', and length scale L' to render the equations non-dimensional.

Let us consider the non-dimensional form of Eqn. (3.2), namely,

$$\frac{\partial c'}{\partial t'} = M' \nabla'^2 \mu'. \tag{A.1}$$

Since we render the dimensional composition variable non-dimensional using Eqn. (3.1), namely,

$$c = \frac{c' - c'_m}{c'_p - c'_m}, \tag{A.2}$$

we obtain $\partial c/\partial c' = 1/(c'_p - c'_m)$. Further, by definition,

$$\begin{aligned} \mu' &= \frac{1}{N'_V} \frac{\delta F'}{\delta c'} \\ &= \frac{1}{N'_V} \frac{\delta F'}{\delta c} \frac{\partial c}{\partial c'} \\ &= \frac{1}{N'_V (c'_p - c'_m)} \frac{\delta F'}{\delta c}. \end{aligned} \tag{A.3}$$

Since the total free energy of the system involves an integration over the volume [73],

we have

$$\begin{aligned} F' &= N'_V \int f(c, \nabla c, \dots) dV' \\ &= \frac{N_V}{L'^3} \int f(c, \nabla c, \dots) dV L'^3 \\ &= N_V \int f(c, \nabla c, \dots) dV. \end{aligned} \tag{A.4}$$

Also, since $\delta F'/\delta c'$ has units of energy per unit volume, the chemical potential $\mu' = (1/N'_V)\ [\delta F'/\delta c']$ has units of energy per atom. Hence,

$$\begin{aligned} \mu &= \frac{\mu'}{E'} = \frac{1}{E'} \frac{L'^3}{N_V} \frac{\delta F}{\delta c'} \frac{E'}{L'^3} \\ &= \frac{1}{N_V} \frac{\delta F}{\delta c'} = \frac{1}{N_V(c'_p - c'_m)} \frac{\delta F}{\delta c} \end{aligned} \tag{A.5}$$

Finally, since

$$\begin{aligned} \frac{\partial c'}{\partial t'} &= \frac{\partial c'}{\partial c} \frac{\partial c}{\partial t'} \\ &= (c'_p - c'_m) \frac{\partial c}{\partial t'} = \frac{(c'_p - c'_m)}{T'} \frac{\partial c}{\partial t}, \end{aligned} \tag{A.6}$$

the non-dimensionalisation of the Eqn. (A.1) becomes

$$\begin{aligned} \frac{\partial c}{\partial t} &= \frac{M'T'}{(c'_p - c'_m)} \nabla'^2 \mu' \\ &= \frac{M'T'}{(c'_p - c'_m) N'_V L'^2} \nabla^2 \mu' \\ &= \frac{M'T'L'^3}{(c'_p - c'_m) N_V L'^2} \nabla^2 \left\{ \frac{\delta F'}{\delta c'} \right\} \\ &= \frac{M'T'L'^3}{(c'_p - c'_m) N_V L'^2} \nabla^2 \left\{ \frac{\delta F}{\delta c'} \frac{E'}{L'^3} \right\} \\ &= \frac{M'T'E'}{(c'_p - c'_m) L'^2} \nabla^2 \left\{ \frac{\delta (F/N_V)}{\delta c'} \right\} \\ &= \frac{M'T'E'}{(c'_p - c'_m) L'^2} \nabla^2 \left\{ \frac{\delta (F/N_V)}{\delta c} \frac{\partial c}{\partial c'} \right\} \\ &= \frac{M'T'E'}{(c'_p - c'_m)^2 L'^2} \nabla^2 \left\{ \frac{\delta (F/N_V)}{\delta c} \right\} \end{aligned} \tag{A.7}$$

Identifying

$$M = \frac{M'T'E'}{(c'_p - c'_m)^2 L'^2}, \tag{A.8}$$

we obtain

$$\frac{\partial c}{\partial t} = M\nabla^2\left[\frac{\delta F/N_V}{\delta c}\right]. \tag{A.9}$$

Making the non-dimensional mobility M unity, we obtain the characteristic time scale as follows:

$$T' = \frac{(c'_p - c'_m)^2 L'^2}{M'E'}. \tag{A.10}$$

Further, using $A'_b = E'$ and $L' = \{\kappa'/A'_b\}^{\frac{1}{2}}$ renders the non-dimensional κ and A_b also unity.

Let us consider an *fcc* crystal with a lattice parameter of 4 Å. Then, the non-dimensional number of atoms per unit volume would be given by $4L'^3/[(4\times10^{-10})^3]$. Since in our phase field model, the scaled non-dimensional interfacial energy is (1/3) [86],

$$\frac{1}{3} = \frac{\gamma}{N_V\kappa^{\frac{1}{2}}}. \tag{A.11}$$

Hence, $\gamma = 4\times(L')^3/(3\times(4\times10^{-10})^3)$ Since interfacial energy is scaled by $E'/(L')^2$, we obtain the characteristic energy as follows:

$$E' = 3\gamma'(4\times10^{-10})^3/4L'. \tag{A.12}$$

Using a characteristic length scale of 1 nm, and assuming the typical interfacial energy to be 0.1 J/m^2, we obtain $E' = A'_b = 4.8\times10^{-21}$ $Joules$.

The non-dimensional mobility M' is related to the non-dimensional diffusivity D' as follows [87]:

$$D' = \frac{\partial^2 f'_0}{\partial c'^2}M'. \tag{A.13}$$

Differentiating the non-dimensional bulk free energy density

$$f'_0 = A'_b\left[\frac{(c'-c'_m)^2(c'-c'_p)^2}{(c'_p-c'_m)^4}\right], \tag{A.14}$$

twice, with respect to c', we obtain

$$\begin{aligned}\frac{\partial^2 f'_0}{\partial c'^2} &= \left[\frac{2A'_b}{(c'_p-c'_m)^4}\right] \\ &\quad [(c'-c'_p)(2c'-c'_m-c'_p) \\ &\quad +(c'-c'_m)(2c'-c'_m-c'_p)+2(c'-c'_m)(c'-c'_p)]\end{aligned} \tag{A.15}$$

Evaluating this quantity at the matrix composition c'_m, we obtain

$$\frac{\partial^2 f'_0}{\partial c'^2} = \frac{2A'_b}{(c'_p - c'_m)^2}. \tag{A.16}$$

Hence,

$$M' = \frac{(c'_p - c'_m)^2}{2A'_b} D'. \tag{A.17}$$

Assuming a typical value of 0.1 for $(c'_p - c'_m)$, and 1.0×10^{-16} m^2/sec for D', we obtain $M' = 1041.6667$ $m^2/(Joule - sec)$

This implies that the characteristic time $T' = [(c'_p - c'_m)^2 L'^2]/[M'E'] = 0.02sec.$

Appendix B

Proof that E denotes the mean strain tensor of the cell

Our aim in this Appendix is to show that that **E** denotes the mean strain tensor of the cell, i.e., derive Eqn. (3.20), viz.,

$$\langle \varepsilon_{ij} \rangle = E_{ij}, \tag{B.1}$$

with the following definition:

$$\langle (\cdot) \rangle = \frac{1}{V} \int_{\Omega} (\cdot) d\Omega, \tag{B.2}$$

where V is the area of the (2D) cell Ω. The derivation below follows Ref. [25], which presents a generalisation of equation (3.20) to cases where the domain Ω contains cavities. To derive Eqn. (3.20), we begin by calculating the strain ε_{ij} from the equation (3.19):

$$\varepsilon_{ij} = \frac{1}{2} \left[\frac{\partial u_i}{\partial r_j} + \frac{\partial u_j}{\partial r_i} \right], \tag{B.3}$$

which gives the following expression:

$$\varepsilon_{ij} = E_{ij} + \frac{1}{2} \left[\frac{\partial u_i^{\star}}{\partial r_j} + \frac{\partial u_j^{\star}}{\partial r_i} \right], \tag{B.4}$$

since we assumed **E** to be symmetric. Further, we have, by definition,

$$\langle \varepsilon_{ij} \rangle = \frac{1}{V} \int_{\Omega} \varepsilon_{ij} d\Omega, \tag{B.5}$$

using Eqn. (B.4) in the above expression, we obtain,

$$\langle \varepsilon_{ij} \rangle = \frac{1}{V} \int_{\Omega} \left\{ E_{ij} + \frac{1}{2} \left[\frac{\partial u_i^\star}{\partial r_j} + \frac{\partial u_j^\star}{\partial r_i} \right] \right\} d\Omega. \tag{B.6}$$

Since $\mathbf{E}$ is a constant,

$$\langle \varepsilon_{ij} \rangle = E_{ij} + \frac{1}{2V} \int_{\Omega} \left[\frac{\partial u_i^\star}{\partial r_j} + \frac{\partial u_j^\star}{\partial r_i} \right] d\Omega. \tag{B.7}$$

If $\partial\Omega$ represent the boundary of Ω, following Gurtin (See p.4 of [88]),

$$\langle \varepsilon_{ij} \rangle = E_{ij} + \frac{1}{2V} \int_{\partial\Omega} (u_i^\star n_j + u_j^\star n_i) d\partial\Omega, \tag{B.8}$$

where, $\mathbf{n}$ is the normal to $\partial\Omega$. Since $\mathbf{u}^\star$ is periodic on Ω and $\mathbf{n}$ would be having opposite signs on the opposite faces of the boundary $\partial\Omega$, the integral vanishes and we get the Eqn. (3.20):

$$\langle \varepsilon_{ij} \rangle = E_{ij}. \tag{B.9}$$

Appendix C

The zeroth order approximation and higher order refinements

The Eqn. (3.35) can be solved in the Fourier space as follows:

$$\int_{\Omega} C^{eff}_{ijkl} \frac{\partial^2 u^{\star}_l(\mathbf{r})}{\partial r_j \partial r_k} \exp\left(-2\pi J \mathbf{g}' \cdot \mathbf{r}\right) d\mathbf{r} = \int_{\Omega} \sigma^T_{ij} \frac{\partial \beta(c)}{\partial r_j} \exp\left(-2\pi J \mathbf{g}' \cdot \mathbf{r}\right) d\mathbf{r}, \tag{C.1}$$

where $\mathbf{g}'$ is the reciprocal space vector, and $J = \sqrt{-1}$. Let us denote $2\pi\mathbf{g}'$ by $\mathbf{g}$ and integrate the above equation by parts once, to obtain

$$\begin{aligned} -Jg_k \textstyle\int_{\Omega} C^{eff}_{ijkl} \frac{\partial u^{\star}_l(\mathbf{r})}{\partial r_j} \exp\left(-J\mathbf{g} \cdot \mathbf{r}\right) d\mathbf{r} \qquad & (C.2) \\ = \\ -Jg_j \int_{\Omega} \sigma^T_{ij} \beta(c) \exp\left(-J\mathbf{g} \cdot \mathbf{r}\right) d\Omega, & \end{aligned}$$

where the boundary terms vanish because of the periodic boundary conditions on the composition c and the strain $\varepsilon^{\star}$. Using the notation $\{(\cdot)\}_{\mathbf{g}}$ for the Fourier transform of $(\cdot)$,

$$Jg_k \int_{\Omega} C^{eff}_{ijkl} \frac{\partial u^{\star}_l(\mathbf{r})}{\partial r_j} \exp\left(-J\mathbf{g} \cdot \mathbf{r}\right) d\mathbf{r} = Jg_j \sigma^T_{ij} \left\{\beta(c)\right\}_{\mathbf{g}}, \tag{C.3}$$

Let us integrate the LHS of the above equation once more by parts (and use the periodic boundary condition on the displacement $u^{\star}$ to get rid of the boundary terms):

$$g_k g_j C^{eff}_{ijkl} \{u^{\star}_l\}_{\mathbf{g}} = -Jg_j \sigma^T_{ij} \{\beta(c)\}_{\mathbf{g}}. \tag{C.4}$$

Defining G_{il}^{-1} as $C_{ijkl}^{eff} g_k g_j$, we can write the solution in the Fourier space as follows:

$$\left\{(u_l^\star)^0\right\}_{\mathbf{g}} = -JG_{il}\sigma_{ij}^T g_j \{\beta(c)\}_{\mathbf{g}}, \tag{C.5}$$

where the superscript on $u_k^\star$ denotes the order of approximation.

C.1 First order approximation

Having the zeroth order approximation it is possible to refine the solution. Let us consider the equation (3.18) again. Let us assume that ΔC_{ijkl} is non-zero and substitute for the zeroth order approximation solution in the second term of the LHS of the equation. We obtain,

$$\begin{aligned} C_{ijkl}^{\mathrm{eff}} \frac{\partial^2 (u_l^\star)^1(\mathbf{r})}{\partial r_j \partial r_k} & \\ = & \\ & C_{ijkl}^{eff} \varepsilon^T \delta_{kl} \frac{\partial \beta(c)}{\partial r_j} \\ & -\Delta C_{ijkl} E_{kl}^0 \frac{\partial \alpha(c)}{\partial r_j} \\ & +\Delta C_{ijkl} \varepsilon^T \delta_{kl} \frac{\partial \{\beta(c)\alpha(c)\}}{\partial r_j} \\ & -\Delta C_{ijkl} \frac{\partial}{\partial r_j} \left(\alpha(c) \frac{\partial (u_l^\star)^0(\mathbf{r})}{\partial r_k} \right), \end{aligned} \tag{C.6}$$

where the superscript 0 on $\mathbf{E}$ denotes that the homogeneous strain is calculated from the zeroth order approximation of solution using the equation (3.28).

The above equation can be solved using Fourier techniques as earlier:

$$\left\{(u_l^\star)^1\right\}_{\mathbf{g}} = -JG_{il}\Lambda_{ij} g_j, \tag{C.7}$$

where

$$\begin{aligned} \Lambda_{ij} \;=\; & \sigma_{ij}^T \{\beta(c)\}_{\mathbf{g}} - \Delta C_{ijmn} E_{mn}^0 \{\alpha(c)\}_{\mathbf{g}} \\ & +\Delta C_{ijmn} \varepsilon^T \delta_{mn} \{\alpha(c)\ \beta(c)\}_{\mathbf{g}} - \Delta C_{ijmn} \left\{ \alpha(c) \frac{\partial (u_m^\star)^0(\mathbf{r})}{\partial r_n} \right\}_{\mathbf{g}} \end{aligned} \tag{C.8}$$

C.2 Higher order approximations

Generalising the above derivation of the first order solution from the zeroth order solution, we can write the nth order solution from the $(n-1)$th order solution as follows:

$$\{(u_l^\star)^n\}_{\mathbf{g}} = -JG_{il}\Lambda_{ij}^{n-1}g_j, \tag{C.9}$$

where

$$\begin{aligned}\Lambda_{ij}^{n-1} &= \sigma_{ij}^T\{\beta(c)\}_{\mathbf{g}} - \Delta C_{ijmn}E_{mn}^{n-1}\{\alpha(c)\}_{\mathbf{g}} \\ &\quad +\Delta C_{ijmn}\varepsilon^T\delta_{mn}\{\alpha[c(\mathbf{r})]\ \beta[c(\mathbf{r})]\}_{\mathbf{g}} - \Delta C_{ijmn}\left\{\alpha[c(\mathbf{r})]\frac{\partial(u_m^\star)^{n-1}(\mathbf{r})}{\partial r_n}\right\}_{\mathbf{g}}\end{aligned} \tag{C.10}$$

C.3 Note on convergence

For linear elastic constitutive laws (as well as perfect plasticity and linear visco-elasticity), the homogenisation problem is known to be well-posed [25]. Further, Hu and Chen [20] also show that each iteration in an iterative procedure of the type described above corresponds to a given order of approximation of the Green function expansion in the formulation of Khachaturyan et al [77]. Thus, our iterative procedure, outlined in this thesis is expected to converge. However, an iterative procedure based on FFT for homogenisation studies is known to converge slowly as the 'contrast' ($\delta \ll 1$) increases [26]; but, as shown in Section 3.7.2, we get, in practise, a surprisingly fast convergence even for cavities ($\delta \ll 1$) using the above methodology (within 9 iterations, albeit for small volume fractions of cavity).

Appendix D

Modified Gibbs-Thomson equation

The equilibrium compositions of the coexisting phases in a two-phase coherent alloy are modified both by the geometry (more specifically, the curvature) of the interface (Gibbs-Thomson or capillarity effect), and by the elastic stresses. All the expressions in this appendix are taken from Abinandanan [89] and Johnson [53] .

Let Δc^m be the deviation of the composition on the matrix side of a curved interface; that is,

$$\Delta c^m = c_R^m - c_\infty^m, \tag{D.1}$$

where c_R^m is the composition of the interface on the matrix side for a precipitate of radius R, and c_∞^m is the composition of the interface on the matrix side when the interface is planar. As noted, there are two contributions to this quantity: one due to capillarity, Δc_c^m, which depends on the curvature of the interface, and another due to elastic stresses, Δc_{el}^m, which depends on the stress and strain fields in the system.

Δc_c^m is given by the Gibbs-Thomson equation:

$$\Delta c_c^m = \frac{\chi^p \gamma}{(c_e^p - c_e^m)\Psi^m} \tag{D.2}$$

where, χ^p is the mean curvature of the interface with respect to the precipitate phase, γ is the interfacial energy density, the c_e^p and c_e^m are the equilibrium compositions of the matrix and precipitate, respectively, when they are separated by a planar

interface, and the quantity Ψ^m is defined as follows:

$$\Psi^m = \left[\frac{\partial^2 f_0}{\partial c^2}\right]_{c_e^m} \tag{D.3}$$

Δc_{el}^m, that is the correction to the Gibbs-Thomson equation (D.2) due to elastic stresses is given as follows:

$$\Delta c_{el}^m = \frac{\chi^p \gamma + \sigma_{ij}^m(\varepsilon_{ij}^m - \varepsilon_{ij}^p) + [\sigma_{ij}^p(\varepsilon_{ij}^p - \varepsilon^T \delta_{ij}) - \sigma_{ij}^m \varepsilon_{ij}^m]/2}{(c_e^p - c_e^m)\Psi^m}, \tag{D.4}$$

where σ and ε are the stress and strain fields respectively.

Let c_∞ be the far-field composition. In terms of c_∞ and, the interfacial compositions for the m and p phases, we can define the 'effective' supersaturation (Δc) as follows:

$$\Delta c = \frac{c_\infty - c_I^m}{c_I^p - c_I^m}. \tag{D.5}$$

Thus, for the same precipitate radius and far-field composition, for the free energy function that we use, we can show that the the denominator remains a constant [53]. Hence, Δc depends on $c_\infty - c_I^m$. Further, since in our case, c_e^p is unity and c_e^m is zero, Δc is given by $c_\infty - \Delta c^m$. In Table D.1, we list Δc_{el}^m, the elastic contribution to the excess matrix interfacial composition around a circular precipitate that has a dilatational misfit of 0.01 with the matrix.

S. No.	System	Δc_{el}^m
1.	Soft precipitate ($\delta = 0.5$)	0.0172
2.	Inclusion ($\delta = 1.0$)	0.0284
3.	Hard precipitate ($\delta = 2.0$)	0.0387

Table D.1: Increase in the interfacial composition on the matrix side due to elastic stresses in our model system

Bibliography

[1] W. C. Johnson. *Influence of elastic stress on phase transformations*. In *Lectures on the theory of phase transformations*, edited by H. I. Aaronson, pp. 35–134. TMS, 184, Thorn Hill Road, Warrendale, Pennsylvania 15086-7528, Second edition (1999).

[2] M. Doi. *Elasticity effects on the microstructure of alloys containing coherent precipitates*. Progress in Materials Science, **40**, pp. 79–180 (1996).

[3] P. Fratzl, O. Penrose, and J. L. Lebowitz. *Modeling of phase separation in alloys with coherent elastic misfit*. Journal of Statistical Physics, **95** (5/6), pp. 1429–1503 (1999).

[4] P. W. Voorhees and W. C. Johnson. *The thermodynamics of elastically stressed crystals*, volume 59 of *Solid state physics: advances in research and applications*, pp. 1–201. Elsevier academic press (2004).

[5] A. J. Ardell and R. B. Nicholson. *On the modulated structure of aged Ni-Al alloys*. Acta Metallurgica, **14**, pp. 1295–1309. (With an appendix on the elastic interaction between inclusions by J.D. Eshelby) (October 1966).

[6] M. Doi, T. Miyazaki, and T. Wakatsuki. *The effects of elastic interaction energy on the γ' precipitate morphology of continuously cooled nickel-base superalloys*. Materials Science and Engineering, **74**, pp. 139–145 (1985).

[7] M. J. Kaufman, P. W. Voorhees, W. C. Johnson, and F. S. Biancaniello. *An elastically induced morphological instability of a misfitting precipitate*. Metallurgical Transactions A, **20A**, pp. 2171–2175 (October 1989).

[8] Y. S. Yoo, D. Yoon, and M. F. Henry. *The effect of elastic misfit strain on the morphological evolution of γ'-precipitates in a model Ni-base superalloy*. Metals and Materials, **1** (1), pp. 47–61 (1995).

[9] J. K. Tien and S. M. Copley. *The effect of uniaxial stress on the periodic morphology of coherent gamma prime precipitates in nickel-base superalloy crystals*. Metallurgical Transactions, **2**, pp. 215–219 (January 1971).

[10] N. Sridhar, J. M. Rickman, and D. J. Srolovitz. *Microstructural stability of stressed lamellar and fiber composites*. Acta Materialia, **45** (7), pp. 2715–2733 (1997).

[11] A. Onuki and H. Nishimori. *Anomalously slow domain growth due to a modulus inhomogeneity in phase-separating alloys*. Physical Review B, **43** (16), pp. 13649–13652 (June 1991).

[12] K. Thornton, J. Ågren, and P. Voorhees. *Modelling the evolution of phase boundaries in solids at the meso- and nano-scales*. Acta Materialia, **51**, pp. 5675–5710 (2003).

[13] A. Onuki. *Ginzburg-Landau approach to elastic effects in the phase separation of solids*. Journal of the Physical Society of Japan, **58** (9), pp. 3065–3068 (September 1989).

[14] A. Onuki. *Long range interactions through elastic fields in phase-separating solids*. Journal of the Physical Society of Japan, **58** (9), pp. 3069–3072 (September 1989).

[15] H. Nishimori and A. Onuki. *Pattern formation in phase-separating alloys with cubic symmetry*. Physical Review B, **42** (1), pp. 980–983 (July 1990).

[16] D. Y. Li and L. Q. Chen. *Shape evolution and splitting of coherent particles under applied stresses*. Acta Materialia, **47** (1), pp. 247–257 (1999).

[17] A. Onuki and A. Furukawa. *Phase transitions of binary alloys with elastic inhomogeneity*. Physical Review Letters, **86** (3), pp. 452–455 (2001).

[18] P. H. Leo, J. S. Lowengrub, and H. J. Jou. *A diffuse interface model for microstructural evolution in elastically stressed solids*. Acta Materialia, **46** (6), pp. 2113–2130 (1998).

[19] J. Zhu, L.-Q. Chen, and J. Shen. *Morphological evolution during phase separation and coarsening with strong inhomogeneous elasticity*. Modelling and Simulation in Materials Science and Engineering, **9**, pp. 499–511 (2001).

[20] S. Y. Hu and L. Q. Chen. *A phase-field model for evolving microstructures with strong elastic inhomogeneity*. Acta Materialia, **49**, pp. 1879–1890 (2001).

[21] Y. M. Jin, Y. U. Wang, and A. G. Khachaturyan. *Three-dimensional phase field microelasticity theory and modeling of multiple cracks and voids*. Applied Physics Letters, **79** (19), pp. 3071–3073 (November 2001).

[22] Y. U. Wang, Y. M. Jin, and A. G. Khachaturyan. *Phase field microelasticity theory and simulation of multiple voids and cracks in single crystals and polycrystals under applied stress*. Journal of Applied Physics, **91** (10), pp. 6435–6451 (May 2002).

[23] Y. U. Wang, Y. M. Jin, and A. G. Khachaturyan. *Three-dimensional phase field microelasticity theory of a complex elastically inhomogeneous solid*. Applied Physics Letters, **80** (24), pp. 4513–4515 (June 2002).

[24] Y. U. Wang, Y. M. Jin, and A. G. Khachaturyan. *Phase field microelasticity theory and modeling of elastically and structurally inhomogeneous solid*. Journal of Applied Physics, **92** (3), pp. 1351–1360 (August 2002).

[25] A. Anthoine. *Derivation of the in-plane elastic characteristics of masonry through homogenization theory*. International Journal of Solids and Structures, **32** (2), pp. 137–163 (1995).

[26] J. C. Michel, H. Moulinec, and P. Suquet. *Effective properties of composite materials with periodic microstructure: a computational approach*. Computer Methods in Applied Mechanics and Engineering, **172**, pp. 109–143 (1999).

[27] H. Moulinec and P. Suquet. *A numerical method for computing the overall response of nonlinear composites with complex microstructure*. Computer Methods in Applied Mechanics and Engineering, **157**, pp. 69–94 (1998).

[28] T. Mura. *Micromechanics of defects in solids*. Kluwer academic publishers, 1982 edition (1998 (Reprint, incorporating minor corrections in 1991)).

[29] A. G. Khachaturyan. *Theory of structural transformations in solids*. John Wiley & Sons, Wiley-Interscience edition (1983).

[30] S. Nemat-Nasser and M. Hori. *Micromechanics: overall properties of heterogeneous materials*. Elsevier Science, Second Revised edition (1999).

[31] M. E. Gurtin. *Configurational forces as basic concepts of continuum physics*. Springer-Verlag, New York, first edition (2000).

[32] J. D. Eshelby. *Elastic inclusions and inhomogeneities*. Progress in Solid Mechanics, **2**, pp. 89–140 (1961).

[33] T. Mura. *Inclusion problems*. Applied Mechanics Reviews, **41** (1), pp. 15–20 (January 1988).

[34] E. S. Fisher. *On the elastic moduli of nickel rich Ni-Al alloy single crystals*. Scripta Metallurgica, **20**, pp. 279–284 (1986).

[35] S. V. Prikhodko, J. D. Carnes, D. G. Isaak, H. Yang, and A. J. Ardell. *Temperature and composition dependence of the elastic constants of Ni_3Al*. Metallurgical and Materials Transactions A, **30A**, pp. 2403–2408 (September 1999).

[36] M. Fährmann, P. Fratzl, O. Paris, E. Fährmann, and W. C. Johnson. *Influence of coherency stress on microstructural evolution in model Ni-Al-Mo alloys*. Acta Metallurgica et Materialia, **43** (3), pp. 1007–1022 (1995).

[37] J. G. Conley, M. E. Fine, and J. R. Weertman. *Effect of lattice disregistry variation on the late stage phase transformation behaviour of precipitates in Ni-Al-Mo alloys*. Acta Metallurgica, **37** (4), pp. 1251–1263 (1989).

[38] Y. Wang, L. Q. Chen, and A. G. Khachaturyan. *Kinetics of strain-induced morphological transformation in cubic alloys with a miscibility gap*. Acta Metallurgica et Materialia, **41** (1), pp. 279–296 (1993).

[39] Y. Wang and A. G. Khachaturyan. *Shape instability during precipitate growth in coherent solids*. Acta Metallurgica et Materialia, **43** (5), pp. 1837–1857 (1995).

[40] J. K. Lee. *Effects of applied stress on coherent precipitates via a discrete atom method*. Metals and Materials, **2** (3), pp. 183–193 (1996).

[41] T. Miyazaki, H. Imamura, H. Mori, and T. Kozakai. *Theoretical and experimental investigations on elastic interactions between γ' precipitates in a Ni-Al alloy*. Journal of Materials Science, **16**, pp. 1197–1203 (1981).

[42] M. Doi, T. Miyazaki, and T. Wakatsuki. *The effect of elastic interaction energy on the morphology of γ' precipitates in nickel-based alloys*. Materials Science and Engineering, **67**, pp. 247–253 (1984).

[43] S. J. Yeom, D. Y. Yoon, and M. F. Henry. *The morphological changes of γ' precipitates in a Ni-8 wt.%Al alloy during their coarsening*. Metallurgical Transactions A, **24A**, pp. 1975–1981 (September 1993).

[44] H. A. Calderon, J. G. Cabanas-Moreno, and T. Mori. *Direct evidence that an apparent splitting pattern of γ' particles in Ni alloys is a stage of coalescence*. Philosophical Magazine Letters, **80** (10), pp. 669–674 (2000).

[45] Y. Yamabe-mitarai and H. Harada. *Formation of a 'splitting pattern' associated with $L1_2$ precipitates in Ir-Nb alloys*. Philosophical Magazine Letters, **82** (3), pp. 109–118 (2002).

[46] A. G. Khachaturyan, S. V. Semenovskaya, and J. W. Morris. *Theoretical analysis of strain-induced shape changes in cubic precipitates during coarsening*. Acta Metallurgica, **36** (6), pp. 1563–1572 (1988).

[47] D. Banerjee, R. Banerjee, and Y. Wang. *Formation of split patterns of γ' precipitates in Ni-Al via particle aggregation*. Scripta Materialia, **41** (9), pp. 1023–1030 (1999).

[48] P.-R. Cha, D.-H. Yeon, and S.-H. Chung. *Phase-field study for the splitting mechanism of coherent misfitting precipitates in anisotropic elastic media*. Scripta Materialia, **52**, pp. 1241–1245 (2005).

[49] M. F. Henry, Y. S. Yoo, D. Y. Yoon, and J. Choi. *The dendritic growth of γ' precipitates and grain boundary serration in a model nickel-base superalloy*. Metallurgical Transactions A, **24A**, pp. 1733–1743 (August 1993).

[50] H. J. Jou, P. H. Leo, and J. S. Lowengrub. *Microstructural evolution in inhomogeneous elastic media*. Journal of Computational Physics, **131**, pp. 109–148 (1997).

[51] D.-H. Yeon, P.-R. Cha, J.-H. Kim, M. Grant, and J.-K. Yoon. *A phase field model for phase transformation in an elastically stressed binary alloy*. Modelling and Simulation in Materials Science and Engineering, **13**, pp. 1–21 (2005).

[52] F. R. N. Nabarro, C. M. Cress, and P. Kotschy. *The thermodynamic driving force for rafting in superalloys*. Acta Materialia, **44** (8), pp. 3189–3198 (1996).

[53] W. C. Johnson. *Precipitate shape evolution under applied stress - thermodynamics and kinetics*. Metallurgical Transactions A, **18A**, pp. 233–247 (February 1987).

[54] W. C. Johnson, M. B. Berkenpas, and D. E. Laughlin. *Precipitate shape transitions during coarsening under uniaxial stress*. Acta Metallurgica, **36** (12), pp. 3149–3162 (1988).

[55] I. Schmidt and D. Gross. *Directional coarsening in Ni-base superalloys: analytical results for an elasticity based model*. Proceedings of Royal Society (London) A, **455**, pp. 3085–3106 (1999).

[56] A. Pineau. *Influence of uniaxial stress on the morphology of coherent precipitates during coarsening – elastic energy considerations*. Acta Metallurgica, **24**, pp. 559–564 (1976).

[57] J. K. Lee. *Studying stress-induced morphological evolution with the Discrete Atom Method*. Journal of Metals, **49** (12), pp. 37–40,58 (1997).

[58] Y. H. Wen, Y. Wang, and L. Q. Chen. *Influence of an applied strain field on microstructural evolution during the $\alpha_2 \rightarrow$ o-phase transformation in Ti-Al-Nb system*. Acta Materialia, **49**, pp. 13–20 (2001).

[59] T. Taniguchi and A. Onuki. *Network domain structure in viscoelastic phase separation*. Physical Review Letters, **77** (24), pp. 4910–4913 (December 1996).

[60] C. Sagui, A. M. Somoza, and R. C. Desai. *Spinodal decomposition in an order-disorder phase transition with elastic fields*. Physical Review E, **50** (6), pp. 4865–4879 (December 1994).

[61] R. H. Torii and S. Balibar. *Helium crystals under stress: the Grinfeld instability*. Journal of Low Temperature Physics, **89** (1/2), pp. 391–400 (1992).

[62] A. G. Cullis, D. J. Robbins, A. J. Pidduck, and P. W. Smith. *The characteristics of strain-modulated surface undulations formed upon epitaxial $Si_{1-x}Ge_x$ alloy layers on Si*. Journal of Crystal Growth, **123**, pp. 333–343 (1992).

[63] J. Berrehar, C. Caroli, C. Lapersonne-Meyer, and M. Schott. *Surface patterns on single-crystal films under uniaxial stress: experimental evidence for Grinfeld instability*. Physical Review B, **46** (20), pp. 13487–13495 (1992).

[64] L. B. Freund and S. Suresh. *Thin film materials: stress, defect formation and surface evolution*. Cambridge University Press, first edition (2003).

[65] V. A. Shchukin and D. Bimberg. *Spontaneous ordering of nanostructures on crystal surfaces*. Reviews of Modern Physics, **71** (4), pp. 1125–1171 (July 1999).

[66] M. A. Grinfeld. *The stress driven instabilities in crystals: mathematical models and physical manifestations*. IMA preprint series 819, Institute for mathematics and its applications, University of Minnesota (June 1991).

[67] R. J. Asaro and W. A. Tiller. *Interface morphology development during stress corrosion cracking: Part I. via surface diffusion*. Metallurgical Transactions, **3** (July), pp. 1789–1796 (1972).

[68] M. A. Grinfeld. *Instability of the separation boundary between a nonhydrostatically stressed elastic body and melt*. Soviet Physics Doklady, **31** (10), pp. 831–834 (1986).

[69] D. J. Srolovitz. *On the stability of surfaces of stressed solids*. Acta Metallurgica, **37** (2), pp. 621–625 (1989).

[70] J. W. Gibbs. *Collected Works*, volume 1. Yale University Press (1948).

[71] J. W. Cahn. *On spinodal decomposition*. Acta Metallurgica, **9**, pp. 795–801 (September 1961).

[72] J. W. Cahn. *Spinodal decomposition*. Transactions of the Metallurgical Society of AIME, **242**, pp. 166–180 (February 1968).

[73] J. W. Cahn and J. E. Hilliard. *Free energy of a nonuniform system I. Interfacial free energy*. Journal of Chemical Physics, **28** (2), pp. 258–267 (February 1958).

[74] S. M. Allen and J. W. Cahn. *Mechanisms of phase transformations within the miscibility gap of Fe-rich Fe-Al alloys*. Acta Metallurgica, **24**, pp. 425–437 (1976).

[75] L.-Q. Chen. *Phase-field models for microstructure evolution*. Annual Reviews of Materials Research, **32**, pp. 113–140 (2002).

[76] W. J. Boettinger, J. A. Warren, C. Beckermann, and A. Karma. *Phase-field simulation of solidification*. Annual Reviews of Materials Research, **32**, pp. 163–194 (2002).

[77] A. G. Khachaturyan, S. Semenovskaya, and T. Tsakalakos. *Elastic strain energy of inhomogeneous solids*. Physical Review B, **52** (22), pp. 15909–15919 (December 1995).

[78] L. Q. Chen and J. Shen. *Applications of semi-implicit Fourier-spectral method to phase field equations*. Computer Physics Communications, **108**, pp. 147–158 (1998).

[79] M. Frigo and S. G. Johnson. *The design and implementation of FFTW3*. Proceedings of the IEEE, **93** (2), pp. 216–231. Special issue on "Program Generation, Optimization, and Platform Adaptation"; also see `http://www.fftw.org/` (2005).

[80] S. J. Wang, R. F. Sekerka, A. A. Wheeler, B. T. Murray, S. R. Coriell, R. J. Braun, and G. B. McFadden. *Thermodynamically-consistent phase-field models for solidification*. Physica D, **69**, pp. 189–200 (1993).

[81] R. Sankarasubramanian, C. S. Jog, and T. A. Abinandanan. *Symmetry-breaking transitions in equilibrium shapes of coherent precipitates: effect of elastic anisotropy and inhomogeneity*. Metallurgical and Materials Transactions A, **33A**, pp. 1083–1090 (April 2002).

[82] J. F. Nye. *Physical properties of crystals*. Oxford at the Clarendon Press, first edition (1957).

[83] M. A. Jawson and R. D. Bhargava. *Two-dimensional elastic inclusion problems*. Proceedings of Cambridge Philosophical Society, **57**, pp. 669–680 (1961).

[84] K. F. Riley, M. P. Hobson, and S. J. Bence. *Mathematical methods for physics and engineering*. Cambridge University Press, low priced 1999 edition (1998).

[85] S. P. Timoshenko and J. N. Goodier. *Theory of elasticity*. Mc-Graw Hill, third edition (1970).

[86] T. A. Abinandanan and F. Haider. *An extended Cahn-Hilliard model for interfaces with cubic anisotropy*. Philosophical Magazine A, **81** (10), pp. 2457–2479 (2001).

[87] R. Mukherjee. *Precipitate growth kinetics: a phase field study*. Master's thesis, Department of Metallurgy, Indian Institute of Science, Bangalore 560 012, INDIA (August 2005).

[88] M. E. Gurtin. *An introduction to continuum mechanics*. Academic press (2003 (First Indian Reprint, 2005)).

[89] T. A. Abinandanan. *Coarsening of elastically interacting coherent particles*. Ph.D. thesis, Department of Metallurgical Engineering and Materials Science, Carnegie Mellon University, Pittsburgh, Pennsylvania (April 1991).